Closed-Form Modeling and Control of Spacecraft Swarms in Eccentric Orbits

Nicholas Delurgio
Dept. of Mechanical Engineering
Stanford University
Stanford, CA 94305
delurgio@stanford.edu

Simone D'Amico
Dept. of Aeronautics & Astronautics
Stanford University
Stanford, CA 94305
damicos@stanford.edu

Abstract*—Spacecraft formation-flying and swarm missions have received great attention in the space sector over the past few decades. Some modern multi-satellite missions require the use of an eccentric orbit to access varying altitudes, new ground tracks, and a lower perturbation environment. The use of a distributed mission architecture becomes more challenging in eccentric orbits due to the increased complexity of relative motion dynamics, and important mission considerations such as passive safety, differential perturbation modeling, and efficient impulsive control become more difficult to resolve in closed-form. This paper introduces a new state representation denoted Eccentric Relative Orbit Elements (EROE) to address these issues. The EROE provide an insightful geometric tie into relative position and velocity in eccentric orbits, revealing closed-form expressions for passive safety. Leveraging the fact that EROE are functions of orbit elements, state transition matrices including differential J2, solar radiation pressure, and third body perturbations are also presented. Finally, this paper maps the EROE state onto an existing impulsive control methodology to compute maneuver schemes in closed-form. Using the advantages provided by the chosen state representation, design and maintenance strategies are proposed for swarms, all of which require little computational effort. These results are applied to the mission design and simulation of a conceptual three-spacecraft swarm mission denoted the Mars Gravity Experiment. Simulation results demonstrate over two orders of magnitude improved positional accuracy over short time periods when using the STMs provided in this paper compared to Yamanaka-Ankersen, and delta-v budgeting is accurate within 0.5% of nonlinear simulation.

TABLE OF CONTENTS

1. INTRODUCTION

Distributed Space Systems (DSS) are of increasing interest to the space community due to their ability to achieve a variety of capabilities either more challenging or not possible with a single spacecraft. Spacecraft formation-flying and swarms are a class of DSS architectures in which multiple spacecraft operate in close proximity to achieve certain objectives. For example, the Starling Formation-Flying Optical Experiment (StarFOX), the Space Weather Atmospheric Reconfigurable Multiscale Experiment (SWARM-EX), and the Virtual Super Optics Reconfigurable Swarm (VISORS) utilize such architectures to enable new optical navigation technologies, perform aeronomy research, and increase focal length of coronagraph imaging, respectively [1] [2] [3]. Note that all the missions above operate in Low Earth Orbit (LEO).

These distributed architectures require additional mission design considerations compared to monolithic architectures such as collision avoidance, inter-satellite communication, and relative orbit design. Furthermore, recent trends indicate that the interest in using eccentric orbits is increasing. The Escape and Plasma Acceleration and Dynamics Explorers (EscaPADE), the Magnetospheric Multiscale Mission (MMS), and the HelioSwarm mission all use eccentric orbits to take magnetosphere measurements at varying altitudes [4] [5] [6]. Other missions such as the Miniaturized Distributed Occulter-Telescope Mission (mDOT) and the Proba-3 mission use eccentric orbits to access lower perturbation environments during precision alignment [7] [8]. Overall, the combination of additional ground tracks and altitudes sometimes makes the use of an eccentric orbit necessary. In addition, the lower perturbation environment in many eccentric orbits offers a significant increase in relative navigation and control accuracy.

The dynamics of relative motion in eccentric orbits are more complicated than in circular orbits. Therefore, a number of challenges which have already been resolved for circular orbits still pose problems for eccentric orbits. One of these issues is the lack of closed-from passive safety guarantees. Passive safety is defined as a guaranteed minimum separation between two spacecraft over a prescribed amount of time and in the absence of control. The most prominent method that provides such a guarantee is Sequential Convex Programming (SCP), but it does not do so in closed-form and requires significant computational effort. Lyapunov control with artificial potentials provides another method, but is limited to using continuous control and relies on "soft" separation constraints which can be violated [9]. Passive safety guarantees for large swarm designs is also a challenge, because the number of checks grows $\mathrm{O}(n^2)$ for n spacecraft.

Another challenge is the closed-form inclusion of perturbations in relative motion dynamics. In this paper, the term closed-form refers to analytical or semi-analytical solutions that are computationally cheap and provide insight into the model. When using a Cartesian state representation such as the Yamanaka-Ankersen state transition matrix (STM), perturbations are typically neglected [10]. Perturbations such as

979-8-3503-0462-6/24/$31.00 ©2024 IEEE

differential J2, solar radiation pressure, and third body effects have significant impacts on relative motion in eccentric orbits, degrading the accuracy of such STMs.

Closed-form passive safety and perturbations are addressed in the literature in circular orbits through the use of Relative Orbit Elements (ROEs). ROEs are state representations defined in terms of orbit elements of two spacecraft. Existing nonlinear ordinary differential equations (ODE) for the drift of orbit elements under perturbations can be substituted into ROE states and linearized in order to acquire more accurate analytical models for relative motion. Some ROE definitions also have convenient ties to relative orbit geometry, which reveal closed-form expressions that guarantee passive safety for a large number of spacecraft [11]. However, the ROEs in the literature fail to provide this latter advantage in eccentric orbits, because the geometric map between these ROEs and Cartesian states becomes prohibitively complicated when generalizing to eccentric orbits. In particular, the expressions which have previously been derived all rely on a normalization by varying orbit radius. This makes it difficult to derive analytical expressions for meaningful design metrics such as minimum separation [12] [13].

This paper addresses the challenges of closed-form modeling and control of close-proximity distributed space systems through the use of a new relative orbit element definition. This definition addresses the geometric mapping problem through its close relation to the integration constants of the Yamanaka-Ankersen STM, which is normalized by semi-major axis rather than orbital radius. We refer to this new state representation as the eccentric relative orbit elements, or EROEs. This simple and fundamental tie between EROEs and relative position and velocity enables the derivation of closed-form guarantees of passive safety, which simplifies swarm design and control in eccentric orbits. In addition, in-plane and out-of-plane motion and control become decoupled when working in EROE states, allowing for these two problems to be addressed separately.

Like all other ROE states, state transition matrices that include perturbations can be derived for the EROEs. This paper considers the three most significant perturbations in eccentric orbits: J2, solar radiation pressure, and third body perturbations. Considering these perturbations in a closed-form manner makes swarm maintenance scheduling more predictable, and reveals interesting formation designs that remove certain modes of motion under perturbations.

Finally, this work demonstrates how reachable set theory can be applied in order to create semi-analytical impulsive maneuver schemes in eccentric orbits. Combining this control methodology with closed-form swarm maintenance enables long term and rapid Δv budgeting.

The closed-form modeling and control solutions provided in this paper are applied to the mission design of a conceptual mission known as the Mars Gravity Experiment (MGE). MGE demonstrates how EROEs can be applied to the design of a swarm mission's relative orbits. A comparison of the closed-form models against nonlinear simulation provides insight into the performance of the state transition matrices and control schemes.

2. BACKGROUND

Orbit Elements

A spacecraft's orbit is typically parameterized in an inertial reference frame around its central body. There are two sets of orbit elements used interchangeably in this paper. The singular orbit elements, denoted by $\boldsymbol{\alpha}$, are a (semi-major axis), e (eccentricity), i (inclination), Ω (right ascension of the ascending node), ω (argument of periapsis), and M (mean anomaly). They are called such because at zero eccentricity, mean anomaly and argument of perigee are not defined. The quasi-nonsingular orbit elements $\boldsymbol{\alpha}^*$ are given as

$$\boldsymbol{\alpha}^* = \begin{bmatrix} a \\ u \\ e_x \\ e_y \\ i \\ \Omega \end{bmatrix} = \boldsymbol{f}(\boldsymbol{\alpha}) = \begin{bmatrix} a \\ M+\omega \\ e\cos(\omega) \\ e\sin(\omega) \\ i \\ \Omega \end{bmatrix}, \tag{1}$$

where u is the mean argument of latitude, and e_x and e_y are the x and y components of the eccentricity vector. $\boldsymbol{\alpha}^*$ is well defined in circular, non-equatorial orbits.

RTN Reference Frame

For spacecraft relative motion, Hill's orbital frame, or the RTN frame, is a common choice in which to parameterize a "deputy" spacecraft's motion with respect to a "chief" spacecraft. The RTN frame's x axis is aligned with the chief's position vector $\boldsymbol{r}$ with respect to its central body. The z axis is aligned with the chief's angular momentum vector, and the y axis completes the right-handed triad. The RTN frame is shown in Figure 1.

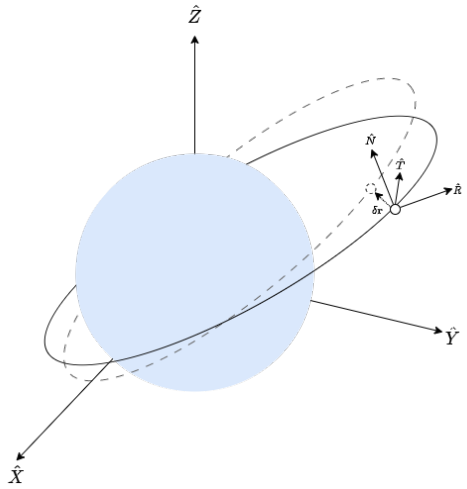

Figure 1: RTN reference frame.

The Cartesian state vector for relative position, $\delta\boldsymbol{r}$, and relative velocity, $\delta\boldsymbol{v}$, of a deputy with respect to its chief in the RTN frame is given as

$$\begin{bmatrix} \delta\boldsymbol{r} \\ \delta\boldsymbol{v} \end{bmatrix} = \begin{bmatrix} x \\ y \\ z \\ \dot{x} \\ \dot{y} \\ \dot{z} \end{bmatrix}, \tag{2}$$

where x, y, and z are the positions along the $\hat{R}, \hat{T}$, and $\hat{N}$ axes, respectively. $\dot{x}, \dot{y}$, and $\dot{z}$ are the time derivatives taken

with respect to the RTN frame. This state representation is used in most relative motion models in the literature.

Clohessy-Wiltshire State Transition Matrix

The first linear model for spacecraft relative motion was introduced in the 1960s by Clohessy and Wiltshire in the context of rendezvous [14]. This model uses the state representation in Equation 2. This state transition matrix (STM) Ψ_{CW} is provided in Equation 64 in the Appendix. This model is initialized by a set of integration constants (IC) K_1 through K_6. The IC can be transformed into initial relative position and velocity coordinates by inverting the matrix in Equation 64. Note that if $K_1 = 0$, spacecraft relative motion is bounded and periodic. If $K_2 = 0$, deputy relative motion is centered around the chief spacecraft.

Relative Orbit Elements

Relative Orbit Elements (ROE) are relative motion state representations that are defined as a function of the orbit elements of two spacecraft. The most straightforward ROE definition is simply the difference between the deputy and chief singular orbit elements. Casotto and Shaub demonstrate that at small inter-spacecraft separations, such a definition has an intrinsic connection to the relative position and velocity of a deputy spacecraft with respect to the chief [15] [16]. The connection between orbit elements and relative Cartesian states is a critical component of relative orbit design.

One popular choice of ROE is introduced by D'Amico in terms of quasi-nonsingular orbit elements [17]. The ROE definition, denoted $\delta\boldsymbol{\alpha}^c$ is provided as

$$\delta\boldsymbol{\alpha}^c = \begin{bmatrix} \delta a^c \\ \delta\lambda^c \\ \delta e_x^c \\ \delta e_y^c \\ \delta i_x^c \\ \delta i_y^c \end{bmatrix} = \begin{bmatrix} (a_d - a)/a \\ u_d - u + (\Omega_d - \Omega)\cos(i) \\ e_{d,x} - e_x \\ e_{d,y} - e_y \\ i_d - i \\ (\Omega_d - \Omega)\sin(i) \end{bmatrix}, \tag{3}$$

where the subscript d indicates deputy orbit elements, and no subscript indicates chief orbit elements. δa is the relative semi-major axis, $\delta\lambda$ is the relative longitude, δe_x and δe_y are the x and y components of the relative eccentricity vector $\delta\boldsymbol{e}$, and δi_x and δi_y are the x and y components of the relative inclination vector $\delta\boldsymbol{i}$. The c superscript is used to distinguish this ROE definition, which is often applied in circular orbits, from other definitions. $\delta\alpha^c$ shares a first order equivalence with the integration constants of the Clohessy-Wiltshire STM through the relation [17]

$$\begin{bmatrix} K_1 \\ K_2 \\ K_3 \\ K_4 \\ K_5 \\ K_6 \end{bmatrix} = \begin{bmatrix} 1 & 0 & 0 & 0 & 0 & 0 \\ \frac{3}{2}(u-u_0) & 1 & 0 & 0 & 0 & 0 \\ 0 & 0 & 1 & 0 & 0 & 0 \\ 0 & 0 & 0 & 1 & 0 & 0 \\ 0 & 0 & 0 & 0 & 1 & 0 \\ 0 & 0 & 0 & 0 & 0 & 1 \end{bmatrix} \begin{bmatrix} \delta a^c \\ \delta\lambda^c \\ \delta e_x^c \\ \delta e_y^c \\ \delta i_x^c \\ \delta i_y^c \end{bmatrix} \tag{4}$$

The term $u - u_0$ represents the elapsed mean argument of latitude of the chief. Due to this relation, $\delta\boldsymbol{\alpha}^c$ is a useful state representation as it provides geometric insight into spacecraft relative motion in circular orbits. This property is not shared by Cartesian state representations. The only time-dependent part of this relation is due to the drift in relative longitude, $\delta\lambda$. $K_2 = \delta\lambda_0$ represents the initial relative longitude, and a nonzero relative semi-major axis, δa, causes $\delta\lambda$ to drift linearly in time.

$\delta\boldsymbol{\alpha}^c$ can be controlled through impulsive maneuvers. In the case of a near-circular orbit, the effects of a $\Delta\boldsymbol{v}$ in the RTN frame applied at a mean argument of latitude u is [18]

$$\Delta\delta\boldsymbol{\alpha}^c = \frac{1}{na}\begin{bmatrix} 0 & 2 & 0 \\ -2 & 0 & 0 \\ \sin(u) & 2\cos(u) & 0 \\ -\cos(u) & 2\sin(u) & 0 \\ 0 & 0 & \cos(u) \\ 0 & 0 & \sin(u) \end{bmatrix} \begin{bmatrix} \Delta v_R \\ \Delta v_T \\ \Delta v_N \end{bmatrix} \tag{5}$$

Notice the full decoupling of in-plane and out-of-plane maneuvers to the first order. This makes control of $\delta\boldsymbol{\alpha}^c$ simpler in near-circular orbits. Although applicable, these equations do not retain this decoupling in eccentric orbits, making control of $\delta\boldsymbol{\alpha}^c$ more challenging [19].

Yamanaka-Ankersen State Transition Matrix

Yamanaka and Ankersen present a generalization of the Clohessy-Wiltshire state transition matrix to eccentric orbits [10]. The original derivation is parameterized in terms of true anomaly, which is not defined in circular orbits. Guffanti, Willis, and D'Amico present a transformation of the original matrix such that it is parameterized in terms of true argument of latitude, $\theta = \omega + \nu$, where ν is the true anomaly [20] [12]. The resultant STM Ψ_{YA} is valid for both circular and eccentric orbits and is given in the Appendix in Equation 65. This model is initialized by a set of integration constants denoted C_1 through C_6. Note that Equation 65 simplifies to Equation 64 at zero eccentricity, because the singular terms go to zero for strictly circular orbits. This form of the Yamanaka-Ankersen STM is considered the state of the art in linear Cartesian models of relative motion, and will be referenced throughout the paper.

3. ECCENTRIC RELATIVE ORBIT ELEMENTS

The Eccentric Relative Orbit Elements (EROE) are introduced in this paper as a new state representation for spacecraft relative motion. Their primary advantage is that they are defined such that they share a first order equivalence with the integration constants of the Yamanaka-Ankersen STM. This feature enables an insightful geometric mapping from EROE states to relative position and velocity in eccentric orbits. This differs from the ROE definition in Equation 3, which only provides such an insight in circular orbits.

Definition

The singular definition of the EROEs is

$$\delta\boldsymbol{\alpha} = \begin{bmatrix} \delta a \\ \delta\lambda \\ \delta e_x \\ \delta e_y \\ \delta i_x \\ \delta i_y \end{bmatrix} = \begin{bmatrix} \eta^2(a_d - a)/a \\ \frac{1}{\eta}(M_d - M) + \eta^2[\omega_d - \omega + (\Omega_d - \Omega)\cos(i)] \\ (e_d - e)\cos(\omega) + \frac{e}{\eta}(M_d - M)\sin(\omega) \\ (e_d - e)\sin(\omega) - \frac{e}{\eta}(M_d - M)\cos(\omega) \\ \eta^2(i_d - i) \\ \eta^2(\Omega_d - \Omega)\sin(i) \end{bmatrix}, \tag{6}$$

where $\eta = \sqrt{1 - e^2}$. $\delta\boldsymbol{\alpha}$ shares a first order equivalence with the integration constants of the Yamanaka-Ankersen STM in Equation 65. This relation, which is derived by inverting Equation 10, is given as

$$\begin{bmatrix} C_1 \\ C_2 \\ C_3 \\ C_4 \\ C_5 \\ C_6 \end{bmatrix} = \begin{bmatrix} 1 & 0 & 0 & 0 & 0 & 0 \\ \frac{3nt}{2\eta^3} & 1 & 0 & 0 & 0 & 0 \\ \frac{3e_y nt}{2\eta^3} & 0 & 1 & 0 & 0 & 0 \\ -\frac{3e_x nt}{2\eta^3} & 0 & 0 & 1 & 0 & 0 \\ 0 & 0 & 0 & 0 & 1 & 0 \\ 0 & 0 & 0 & 0 & 0 & 1 \end{bmatrix} \begin{bmatrix} \delta a \\ \delta\lambda \\ \delta e_x \\ \delta e_y \\ \delta i_x \\ \delta i_y \end{bmatrix} \tag{7}$$

where n is the mean motion of the chief and t is the elapsed time. In eccentric orbits, three of the EROE drift under a nonzero δa and must be propagated back to their initial conditions to match with the integration constants. This is expected because $\delta\lambda$, δe_x and δe_y are all functions of mean anomaly. More information about these dynamics is given in Section 3-C.

Geometry

Substituting Equation 7 into 65 provides a direct map between EROE and relative position and velocity in the RTN frame with associated insight into the geometry of relative motion. $\delta\boldsymbol{e}$ and $\delta\boldsymbol{i}$ can also be expressed in phase-amplitude form as

$$\begin{aligned}\delta\boldsymbol{e} &= \begin{bmatrix}\delta e_x\\ \delta e_y\end{bmatrix} = \begin{bmatrix}\delta e\cos(\psi)\\ \delta e\sin(\psi)\end{bmatrix},\\ \delta\boldsymbol{i} &= \begin{bmatrix}\delta i_x\\ \delta i_y\end{bmatrix} = \begin{bmatrix}\delta i\cos(\phi)\\ \delta i\sin(\phi)\end{bmatrix},\end{aligned} \tag{8}$$

where δe and δi are the L2 norms of $\delta\boldsymbol{e}$ and $\delta\boldsymbol{i}$, and ψ and ϕ are the phase angles of the relative eccentricity and inclination vectors which are computed by an arctangent. Substituting Equation 8 into the Yamanaka-Ankersen STM in Equation 65 yields a map between EROE states and relative position as

$$\begin{aligned}\frac{x}{a} &= \frac{1}{k}\delta a - \delta e\cos(\theta-\psi)\\ \frac{y}{a} &= \frac{1}{k}\delta\lambda + (\frac{1}{k}+1)\delta e\sin(\theta-\psi)\\ \frac{z}{a} &= \frac{1}{k}\delta i\sin(\theta-\phi)\end{aligned} \tag{9}$$

Note that $k = 1 + e_x\cos(\theta) + e_y\sin(\theta) = 1 + e\cos(\nu)$. Equation 9 is worth comparing and contrasting with the maps of other ROE definitions. The ROEs introduced by Sullivan and D'Amico provide a geometric map in eccentric orbits as well; however, their Cartesian states are normalized by varying orbit radius [13]. The same applies to the map between the ROEs in Equation 3 and relative position in eccentric orbits, as shown by Willis and D'Amico [12]. The fact that Equation 9 is normalized by semi-major axis rather than radius is a major advantage of the ROE definition in this paper, along with the increased simplicity of these equations compared to other mappings in the literature.

The geometry defined by Equation 9 for $\delta a = 0$ is shown in Figures 2 and 3.

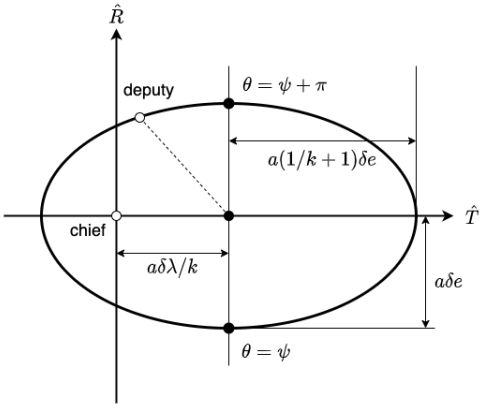

Figure 2: Relative position is depicted in the orbit plane of the chief (RT) for a fixed value of k.

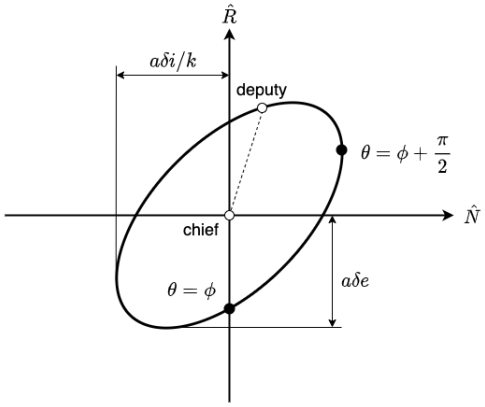

Figure 3: Relative position is depicted in the plane perpendicular to along-track (T) for a fixed value of k.

In circular orbits, $k = 1$ and the motion of the deputy follows an elliptical path around the chief in both the RT and RN planes. However, in eccentric orbits, k causes these ellipses to osculate. Both along-track and cross-track motion gets compressed and expanded over the course of an orbit, with k reaching a minimum value of $1 - e$ at $\nu = \pi$ and a maximum value of $1 + e$ at $\nu = 0$. Examples of the resultant geometry are given by Willis for IC states [12], and in Figure 4 for different phase parameters $\omega - \psi$ and eccentricities e.

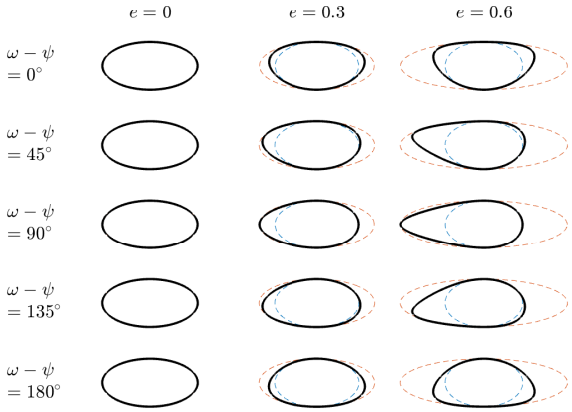

Figure 4: In-plane relative motion for different $\delta\boldsymbol{e}$ phases and absolute orbit eccentricities.

Keplerian Dynamics

As discussed in Section 3-A, $\delta\lambda$, δe_x, and δe_y all drift under Keplerian dynamics when $\delta a \neq 0$. These dynamics are given as

$$\begin{bmatrix}\delta a\\ \delta\lambda(t)\\ \delta e_x(t)\\ \delta e_y(t)\\ \delta i_x\\ \delta i_y\end{bmatrix} = \begin{bmatrix}1 & 0 & 0 & 0 & 0 & 0\\ -\frac{3nt}{2\eta^3} & 1 & 0 & 0 & 0 & 0\\ -\frac{3e_y nt}{2\eta^3} & 0 & 1 & 0 & 0 & 0\\ \frac{3e_x nt}{2\eta^3} & 0 & 0 & 1 & 0 & 0\\ 0 & 0 & 0 & 0 & 1 & 0\\ 0 & 0 & 0 & 0 & 0 & 1\end{bmatrix}\begin{bmatrix}\delta a\\ \delta\lambda(0)\\ \delta e_x(0)\\ \delta e_y(0)\\ \delta i_x\\ \delta i_y\end{bmatrix}, \tag{10}$$

where $n = \sqrt{\mu/a^3}$ is the mean motion. Note the similarity between Equations 10 and 7, where the IC map represents

a back-propagation and the Keplerian dynamics represent a forward-propagation. In circular orbits, it can also be observed that only $\delta\lambda$ will drift under Keplerian dynamics. The direction of $\delta\boldsymbol{e}$ drift is determined by the location of the argument of periapsis ω. As ω rotates due to J2 perturbations (see Section 5), the effect of a nonzero δa will vary greatly in eccentric orbits.

Quasi-Nonsingular Definition

A limitation of the EROE definition in Equation 6 is that it is not defined in circular orbits. Some missions, which might transition between circular and eccentric orbits, would find a quasi-nonsingular ROE state useful. The quasi-nonsingular definition of the EROE is given in Equation 66 in the Appendix. $\delta\boldsymbol{\alpha}^*$ shares a first order equivalence with $\delta\boldsymbol{\alpha}$ and therefore the map to Yamanaka-Ankersen integration constants in Equation 7 is still valid. Note that at small eccentricities, $\delta\boldsymbol{\alpha}^*$ reduces to $\delta\boldsymbol{\alpha}^c$ as $\mathrm{O}(e^2)$ terms go to zero. In fact, this definition represents a generalization of $\delta\boldsymbol{\alpha}^c$ to an orbit of arbitrary eccentricity. Nevertheless, the complexity of Equation 66 shows that using singular orbit elements provides a more natural EROE definition. Therefore, this paper will use the singular definition of the EROE, $\delta\boldsymbol{\alpha}$. All equations derived for $\delta\boldsymbol{\alpha}$ will also apply to $\delta\boldsymbol{\alpha}^*$ in the first order.

4. PASSIVE SAFETY

This section addresses the problem of passive safety in eccentric orbits in closed-form by providing guarantees of a minimum inter-spacecraft separation analytically. This is done separately for in-plane motion and out-of-plane motion. A discussion of how swarms can be designed to incorporate these passive safety guarantees in $\mathrm{O}(n)$ time is also included in Section 4-C.

Out-of-Plane Passive Safety

If $\delta a = 0$, Equation 9 can be rewritten in matrix notation for out-of-plane position as

$$\begin{bmatrix} x \\ z \end{bmatrix} = a \begin{bmatrix} -\delta e_x & -\delta e_y \\ -\frac{\delta i_y}{k} & \frac{\delta i_x}{k} \end{bmatrix} \begin{bmatrix} \cos(\theta) \\ \sin(\theta) \end{bmatrix} \tag{11}$$

The minimum singular value of this matrix is the minimum separation in the RN plane. This can be expressed analytically as

$$\delta r_{RN}^{\min}(k) = \frac{\sqrt{2}a \left| \delta\boldsymbol{e} \cdot \frac{\delta\boldsymbol{i}}{k} \right|}{\left[(\delta e)^2 + \left(\frac{\delta i}{k} \right)^2 + \left| \delta\boldsymbol{e} + \frac{\delta\boldsymbol{i}}{k} \right| \cdot \left| \delta\boldsymbol{e} - \frac{\delta\boldsymbol{i}}{k} \right| \right]^{1/2}} \tag{12}$$

In circular orbits where $k = 1$, this expression represents the true minimum separation between two spacecraft in the RN plane. However, it is most convenient to set k to its maximum value, $1 + e$, in eccentric orbits. This yields the expression

$$\delta r_{RN}^{\min,LB} = \frac{\sqrt{2}a \left| \delta\boldsymbol{e} \cdot \frac{\delta\boldsymbol{i}}{1+e} \right|}{\left[(\delta e)^2 + \left(\frac{\delta i}{1+e} \right)^2 + \left| \delta\boldsymbol{e} + \frac{\delta\boldsymbol{i}}{1+e} \right| \cdot \left| \delta\boldsymbol{e} - \frac{\delta\boldsymbol{i}}{1+e} \right| \right]^{1/2}} \tag{13}$$

Equation 13 represents a lower bound on the separation between two spacecraft, rather than the true minimum. From here, a sufficient condition for passive safety in the RN plane can be computed as

$$|\cos(\psi - \phi)| \geq \frac{\epsilon(1+e)}{a\delta e \delta i} \sqrt{(\delta e)^2 + \left(\frac{\delta i}{1+e} \right)^2 - \left(\frac{\epsilon}{a} \right)^2}, \tag{14}$$

where ϵ is a minimum distance requirement. This expression is a conservative condition for passive safety; if the value of k at which minimum separation occurs is known, that value can be substituted in place of $1 + e$ to yield a more relaxed condition. It is worth noting that if ω is precessing, then this condition is tight. In other words, there is a value of ω for which this lower bound yields the true minimum separation.

In-plane Passive Safety

Passive safety can also be achieved in-plane. Koenig and Guffanti present derivations to achieve in-plane passive safety for circular and eccentric orbits, respectively [18] [20]. The condition of passive safety in the RT plane for the EROEs is

$$|\delta\lambda| \begin{cases} \geq (1+k)\delta e + \frac{\epsilon}{a} & \text{if not encircling} \\ \leq \begin{cases} \sqrt{(1+2k)(\delta e^2 - \frac{\epsilon}{a^2})} & \text{if } \frac{\epsilon}{a} \leq \delta e < \frac{1+k}{k}\frac{\epsilon}{a} \\ (1+k)\delta e - \frac{\epsilon}{a} & \text{if } \delta e \geq \frac{1+k}{k}\frac{\epsilon}{a} \end{cases} & \text{if encircling} \end{cases} \tag{15}$$

By inspection of Equation 15, a lower-bound over an orbit can be achieved by substituting $k = 1 + e$ for the not-encircling case, and $k = 1 - e$ for the encircling case. Doing so yields

$$|\delta\lambda| \begin{cases} \geq (2+e)\delta e + \frac{\epsilon}{a} & \text{if not encircling} \\ \leq \begin{cases} \sqrt{(3-2e)(\delta e^2 - \frac{\epsilon}{a^2})} & \text{if } \frac{\epsilon}{a} \leq \delta e < \frac{2-e}{1-e}\frac{\epsilon}{a} \\ (2-e)\delta e - \frac{\epsilon}{a} & \text{if } \delta e \geq \frac{2-e}{1-e}\frac{\epsilon}{a} \end{cases} & \text{if encircling} \end{cases} \tag{16}$$

Passive Safety for N-Spacecraft Swarms

The number of passive safety checks grows with the square of the number of spacecraft, which can be prohibitively complicated when considering more than three spacecraft. However, there are certain formation designs that guarantee passive safety among all members in a swarm, and only require one passive safety check per spacecraft. These formations are enabled by the geometric properties of the EROE and are much easier to design.

Out-of-Plane—The first design utilizes RN-plane separation to guarantee passive safety. Let N be the number of deputies, and $\delta\boldsymbol{\alpha}_i$ be the EROE for deputy i where $i = 1, ..., N$. First, periodic motion is enforced for all members of the swarm as

$$\delta a_i = 0 \text{ for } i = 1, ..., N \tag{17}$$

The strategy for RN-separated swarms it to make the designed phase angles ψ_{des} and ϕ_{des} equal within a certain tolerance for each deputy as

$$\begin{aligned} \psi_i &= \psi_{des} \text{ for } i = 1, .., N \\ \phi_i &= \phi_{des} \text{ for } i = 1, .., N \end{aligned} \tag{18}$$

In order to guarantee separation between all deputies, δe and δi must be scaled appropriately to ensure minimum distance. Let $\delta\boldsymbol{\alpha}_{jk}$ be the EROE of deputy j with respect to k, where $j = 1, ..., N-1$ and $k = j+1, ..., N$. This swarm can be designed with a minimum separation between closest deputies, where the next closest deputy is defined as the one with the next greatest EROE magnitudes for δe and δi. This can be expressed as

$$\begin{aligned} \delta e_{jk} &= ||\delta\boldsymbol{e}_j - \delta\boldsymbol{e}_k|| \geq \delta e_{min} \\ \delta i_{jk} &= ||\delta\boldsymbol{i}_j - \delta\boldsymbol{i}_k|| \geq \delta i_{min} \end{aligned} \tag{19}$$

where δe_{min} and δi_{min} are design parameters. Since the phase angles for all spacecraft are the same, Equation 19 ensures that δe_{min} and δi_{min} are satisfied for all spacecraft, not just the next closest deputy. Any choice of δe_{min} and δi_{min} that satisfies Equation 14 given ψ_{des} and ϕ_{des} is valid.

These four design parameters $\psi_{des}, \phi_{des}, \delta e_{min}, \delta i_{min}$ can be iterated through until Equation 14 is satisfied. If ψ_{des} and ϕ_{des} are unconstrained by other design requirements, then setting the two vectors to be parallel or anti-parallel yields $|\cos(\psi_{des} - \phi_{des})| = 1$, maximizing the left-hand side of Equation 14. Doing so provides the minimum values of δe_{min} and δi_{min} as

$$\begin{aligned} \delta e_{min} &\geq \frac{\epsilon}{a} \\ \delta i_{min} &\geq \frac{\epsilon}{a}(1+e) \end{aligned} \tag{20}$$

Using these lower bounds for δe_{min} and δi_{min} maximizes the swarm formation density. Keeping the magnitudes of δe_{min} and δi_{min} small also can reduce the maneuver magnitudes in the case of swarm maintenance (see Section 6). Importantly, applying Equations 17, 18, and 19 only requires one check per deputy, keeping the design of large swarms manageable. An example passively safe swarm design is given in Figure 5, with fixed swarm spacing ($\delta e_{jk} = \delta e_{min}, \delta i_{jk} = \delta i_{min}$).

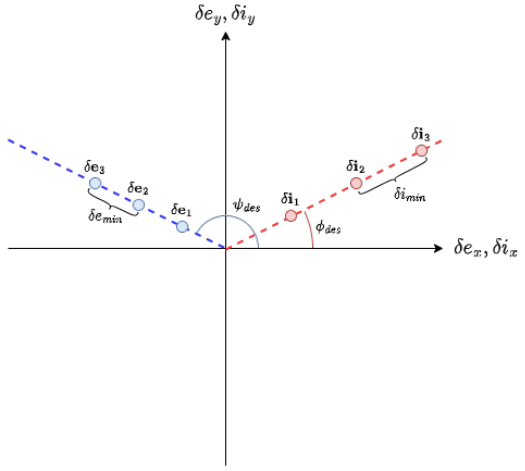

Figure 5: Example RN-plane swarm design for three spacecraft. This design has inter-spacecraft EROE separated by δe_{min} and δi_{min}, while sharing the same phase angles ψ_{des} and ϕ_{des}.

In-Plane—The second swarm design methodology utilizes RT-plane minimum separation to ensure passive safety between all members. Equation 17 still applies to this design to ensure motion is periodic. Although $\delta \boldsymbol{i}$ is not relevant here, a minimum separation threshold in the $\delta \boldsymbol{e}$ plane must be enforced as follows:

$$\delta e_{jk} = ||\delta \boldsymbol{e}_j - \delta \boldsymbol{e}_k|| \geq \delta e_{min} \geq \frac{\epsilon}{a} \tag{21}$$

As shown by Koenig and Guffanti [18] [21], the highest density formation is achieved by placing the relative eccentricity vectors in a grid of equilateral triangles. This can be expressed mathematically for spacecraft j as

$$\delta \boldsymbol{e}_j = \delta e_{min} \begin{bmatrix} W_j \cos(\psi_{des}) + X_j \cos(\psi_{des} + \frac{\pi}{3}) \\ W_j \sin(\psi_{des}) + X_j \sin(\psi_{des} + \frac{\pi}{3}) \end{bmatrix}, \tag{22}$$

where ψ_{des} is a design choice, and W_j and X_j are integers. Both W_j and X_j cannot be zero simultaneously, and a spacecraft k cannot have $W_k = W_j$ and $X_k = X_j$ simultaneously. Such a design yields the geometry in Figure 6.

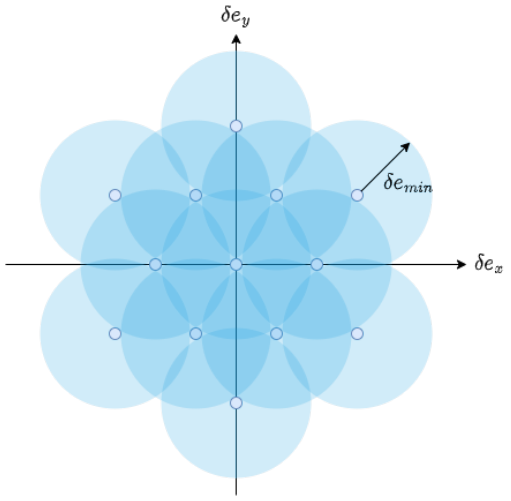

Figure 6: Example $\delta \boldsymbol{e}$ distribution for RT-plane swarm design. This design has inter-spacecraft EROE separated by δe_{min}.

With this relative eccentricity vector design, in-plane passive safety is guaranteed for the entire swarm by enforcing Equation 16 as [18]

$$|\delta\lambda| \leq \frac{g(a, e, \delta e_{min}, \epsilon)}{2} \tag{23}$$

where

$$g(\cdot) = \begin{cases} \sqrt{(3-2e)(\delta e_{min}^2 - \frac{\epsilon}{a^2})} & \text{if } \frac{\epsilon}{a} \leq \delta e_{min} < \frac{2-e}{1-e}\frac{\epsilon}{a} \\ (2-e)\delta e_{min} - \frac{\epsilon}{a} & \text{if } \delta e_{min} \geq \frac{2-e}{1-e}\frac{\epsilon}{a} \end{cases} \tag{24}$$

This design requires that all deputies are encircling the chief, which can constrain the number of spacecraft able to be placed in this formation.

5. Differential Perturbations

There is abundant astrodynamics literature that provides nonlinear differential equations for absolute orbit elements subject to various perturbations [22] [23] [24]. Such ODE can be substituted into the time derivative of any set of ROE to create a nonlinear differential equation for ROE relative motion, in the form

$$\delta \dot{\boldsymbol{\alpha}} = \boldsymbol{f}(\boldsymbol{\alpha}_d, \boldsymbol{\alpha}_c, \boldsymbol{P}), \tag{25}$$

where $\boldsymbol{P}$ is a set of force model parameters. These ODE can be linearized around zero separation ($\boldsymbol{\alpha} = \boldsymbol{\alpha}_d$ or $\delta\boldsymbol{\alpha} = \boldsymbol{0}$) to create linear models for relative motion. In general, the most straightforward way to do this for ROE states is by applying the chain rule derivative as

$$\delta \dot{\boldsymbol{\alpha}} \approx \mathbf{A}(\boldsymbol{\alpha})\delta\boldsymbol{\alpha}, \tag{26}$$

where

$$\mathbf{A}(\boldsymbol{\alpha}) = \frac{\partial \delta\dot{\boldsymbol{\alpha}}}{\partial \boldsymbol{\alpha}_d}\bigg|_{\boldsymbol{\alpha}_d = \boldsymbol{\alpha}} \left(\frac{\partial \delta\boldsymbol{\alpha}}{\partial \boldsymbol{\alpha}_d}\bigg|_{\boldsymbol{\alpha}_d = \boldsymbol{\alpha}} \right)^{-1} \tag{27}$$

If $\mathbf{A}$ is time invariant, it can be solved exactly via a matrix exponential. If not, other methods are available which will be discussed on a case-by-case basis for the perturbations addressed in this paper.

The three most relevant perturbations for formation-flying missions in eccentric orbits are J2, solar radiation pressure, and third-body effects. J2 is especially relevant when periapsis resides at low altitudes. The latter two are important in high eccentricity orbits (HEO), which are a popular formation-flying mission destination [5] [6] [8]. Atmospheric drag is neglected from consideration in this paper. Koenig provides closed-form solutions for relative motion dynamics subject to differential drag [25].

J2 Perturbations

The secular variation of mean absolute orbit elements under the influence of J2 are given as [26]

$$\dot{\boldsymbol{\alpha}}_{J2} = \begin{bmatrix} \dot{a} \\ \dot{e} \\ \dot{i} \\ \dot{\Omega} \\ \dot{\omega} \\ \dot{M} \end{bmatrix}_{J2} = \kappa \begin{bmatrix} 0 \\ 0 \\ 0 \\ -2\cos(i) \\ 5\cos^2(i) - 1 \\ \eta\left(3\cos^2(i) - 1\right) \end{bmatrix}, \tag{28}$$

where $\kappa = \frac{3}{4}\frac{J_2 R^2 \mu^{1/2}}{a^{7/2}\eta^4}$, R is the radius of the central body, and J_2 is the oblateness coefficient of the central body. The nonlinear effects of J2 perturbations on the EROE can be easily computed by substituting Equation 28 into the time derivative of Equation 6. Unfortunately, direct linearization of these equations does not provide a time-invariant plant matrix. However, a set of ROE that yields a time-invariant plant under J2 is provided by Koenig et al. Using this property, an STM for this ROE definition is derived [27]. Therefore, a first-order map between their ROE state and the EROE can be applied pre- and post-propagation in order to derive a J2 STM for the EROE, which is computed as

$$\mathbf{\Phi}^2 = (\mathbf{M}_2^1)^{-1}\mathbf{\Phi}^1\mathbf{M}_2^1, \tag{29}$$

where $\mathbf{M}_2^1$ is the first order map from ROE definition 2 to ROE definition 1. In this case, $\mathbf{\Phi}^1$ represents the STM derived by Koening, $\mathbf{\Phi}^2 = \mathbf{\Phi}_{J2+kep}$ is the STM for the EROE, and $\mathbf{M}_2^1$ can be computed via a chain rule as

$$\mathbf{M}_2^1(\boldsymbol{\alpha}) = \left.\frac{\partial \delta\boldsymbol{\alpha}^1}{\partial \boldsymbol{\alpha}_d}\right|_{\boldsymbol{\alpha}_d=\boldsymbol{\alpha}} \left(\left.\frac{\partial \delta\boldsymbol{\alpha}^2}{\partial \boldsymbol{\alpha}_d}\right|_{\boldsymbol{\alpha}_d=\boldsymbol{\alpha}}\right)^{-1}, \tag{30}$$

where $\delta\boldsymbol{\alpha}^1$ is the first ROE definition, and $\delta\boldsymbol{\alpha}^2$ is the second ROE definition. Using this method, the J2 STM (including Keplerian dynamics) for EROE is

$$\delta\boldsymbol{\alpha}(t) = \mathbf{\Phi}_{J2+kep}(t)\delta\boldsymbol{\alpha}(0) \tag{31}$$

where $\mathbf{\Phi}_{J2+kep}$ is provided in Equation 67 in the Appendix. Inspection of this STM's form reveals that there is a long period rotation as well as a nonlinear change in amplitude on $\delta\boldsymbol{e}$. This change can be negative in short time horizons, but is always positive over long horizons. $\delta\lambda$ and δi_y only experience a secular effect. These effects are shown in Figure 7.

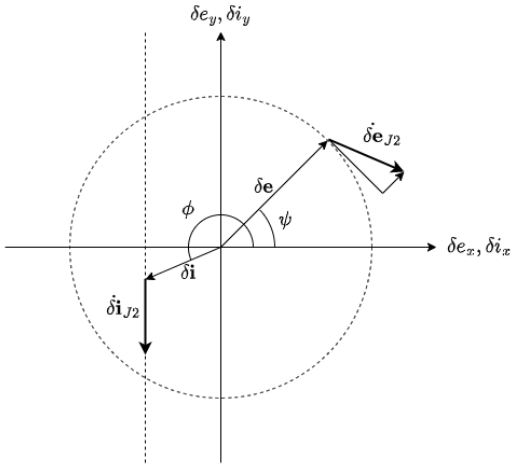

Figure 7: Drift of $\delta\boldsymbol{e}$ and $\delta\boldsymbol{i}$ under J2 perturbations.

A growth in δe causes a spiraling effect on the relative eccentricity vector, which results in the spacecraft drifting apart. A decrease could violate a minimum separation requirement. This is the only additional J2 mode present in eccentric orbits compared to circular orbits, but it can pose a challenge for swarm maintenance. Methods to manage this mode are discussed in Section 6.

Solar Radiation Pressure Perturbations

Solar Radiation Pressure (SRP) is an important perturbation in high eccentricity orbits, and can cause significant ROE drift during apoapsis passes. This section details the derivation methodology, assumptions, and practical applications of the SRP STM.

Cook and Guffanti present a derivation of the nonlinear ODE for secular and long-periodic effects of SRP on mean orbit elements as [28] [21]

$$\dot{\boldsymbol{\alpha}}_{srp} = \begin{bmatrix} \dot{a} \\ \dot{e} \\ \dot{i} \\ \dot{\Omega} \\ \dot{\omega} \\ \dot{M} \end{bmatrix}_{srp} = \gamma_{srp} B_{srp} \sqrt{a} \begin{bmatrix} 0 \\ -\eta(-\mathcal{A}\sin(\omega) + \mathcal{B}\cos(\omega)) \\ \frac{e\cos(\omega)}{\eta}\mathcal{C} \\ \frac{e\sin(\omega)}{\eta}\frac{\mathcal{C}}{\sin(i)} \\ \frac{\eta}{e}(\mathcal{A}\cos(\omega) + \mathcal{B}\sin(\omega)) - \frac{e\sin(\omega)}{\eta}\frac{\cos(i)}{\sin(i)}\mathcal{C} \\ -(3e + \frac{\eta^2}{e})(\mathcal{A}\cos(\omega) + \mathcal{B}\sin(\omega)) \end{bmatrix}, \tag{32}$$

where γ_{srp} is the solar radiation pressure coefficient:

$$\gamma_{srp} = \frac{3}{2\sqrt{\mu}}\frac{\Psi_\odot}{C_\odot}\left(\frac{1\text{ AU}}{r_\odot}\right)^2, \tag{33}$$

where $\Phi_\odot = 1367\frac{\text{W}}{\text{m}^2}$ is the solar flux at 1 AU from the Sun, $C_\odot$ is the speed of light, and $r_\odot$ is the distance between the sun and the central body. $B_{srp} = \frac{C_r A_r}{m}$ is the SRP ballistic coefficient, where C_r is the reflectivity coefficient, A_r is the cross-sectional area that is illuminated, and m is the mass of

the spacecraft. $\mathcal{A}, \mathcal{B}, \mathcal{C}$ are given as

$$\begin{aligned}\mathcal{A} &= \cos(\Omega - \Omega_\odot)\cos(\theta_\odot) + \cos(i_\odot)\sin(\theta_\odot)\sin(\Omega - \Omega_\odot) \\ \mathcal{B} &= \cos(i)[-\sin(\Omega - \Omega_\odot)\cos(\theta_\odot) \\ &\quad + \cos(i_\odot)\sin(\theta_\odot)\cos(\Omega - \Omega_\odot)] + \sin(i)\sin(i_\odot)\sin(\theta_\odot) \\ \mathcal{C} &= \sin(i)[\sin(\Omega - \Omega_\odot)\cos(\theta_\odot) \\ &\quad - \cos(i_\odot)\sin(\theta_\odot)\cos(\Omega - \Omega_\odot)] + \cos(i)\sin(i_\odot)\sin(\theta_\odot),\end{aligned} \tag{34}$$

where $\odot$ represents the fictitious orbit elements of the sun with respect to the central body inertial reference frame.

This work builds off of the contributions of Guffanti, who introduced an STM including differential SRP for the ROE defined in Equation 3. In order to do this, ΔB_{srp}, the difference between the deputy and chief ballistic coefficient, must be included in the state. This results in a plant matrix with the form

$$\mathbf{A}_{srp} = \begin{bmatrix} \frac{\partial \delta \dot{\boldsymbol{\alpha}}_{srp}}{\partial \delta \boldsymbol{\alpha}}\Big|_{\delta\boldsymbol{\alpha}=\mathbf{0}^{6\times1}} & \frac{\partial \delta \dot{\boldsymbol{\alpha}}_{srp}}{\partial \Delta B_{srp}}\Big|_{\Delta B_{srp}=0} \\ \mathbf{0}^{1\times6} & 0 \end{bmatrix} \tag{35}$$

$\frac{\partial \delta \dot{\boldsymbol{\alpha}}_{srp}}{\partial \Delta B_{srp}}\Big|_{\Delta B_{srp}=0}$ is the dominant term in this plant matrix, because the difference in ballistic coefficient is much more influential than the position difference between two close-by spacecraft with respect to the Sun. Therefore, we can reasonably set $\frac{\partial \delta \dot{\boldsymbol{\alpha}}_{srp}}{\partial \delta \boldsymbol{\alpha}}\Big|_{\delta\boldsymbol{\alpha}=\mathbf{0}^{6\times1}} = \mathbf{0}^{6\times6}$ for this plant matrix.

For the ROE in Equation 3, Guffanti derived a plant matrix for secular, long-periodic, differential SRP, assuming no change in ΔB_{srp} as [21]

$$\mathbf{A}^c_{srp}(\boldsymbol{\alpha}) = \gamma_{srp}\sqrt{a}\begin{bmatrix} & 0 \\ & -\frac{2e^2+1-\eta}{e^2}(\mathcal{A}e_x + \mathcal{B}e_y) \\ & -\eta\mathcal{B} + \frac{e_y^2}{\eta}\frac{\cos(i)}{\sin(i)}\mathcal{C} \\ \mathbf{0}^{7\times6} & \eta\mathcal{A} - \frac{e_x e_y}{\eta}\frac{\cos(i)}{\sin(i)}\mathcal{C} \\ & \frac{e_x}{\eta}\mathcal{C} \\ & \frac{e_y}{\eta}\mathcal{C} \\ & 0 \end{bmatrix} \tag{36}$$

Unlike J2, there has not been a ROE definition discovered that provides a time-invariant plant matrix under the influence of differential SRP. This is because five of the absolute orbit element states are affected by SRP, while J2 has only three. However, by assuming constant chief orbit elements and fictitious sun orbit elements, $\mathbf{A}^c_{srp}$ is nilpotent and the corresponding state transition matrix can be computed as

$$\boldsymbol{\Phi}^c_{srp}(t) = \mathbf{I}^{7\times7} + \mathbf{A}^c_{srp}t \tag{37}$$

Using this relation, the differential SRP STM for the EROEs is

$$\boldsymbol{\Phi}_{srp} = (\mathbf{M}^{\delta\boldsymbol{\alpha}^c}_{\delta\boldsymbol{\alpha}})^{-1}\boldsymbol{\Phi}^c_{srp}\mathbf{M}^{\delta\boldsymbol{\alpha}^c}_{\delta\boldsymbol{\alpha}}, \tag{38}$$

where $\mathbf{M}^{\delta\boldsymbol{\alpha}^c}_{\delta\boldsymbol{\alpha}}$ is the first order map from the IC in the Yamanaka-Ankersen STM to the IC in the Clohessy-Wiltshire STM, and therefore a map from the EROEs in Equation 6 to the ROEs in Equation 3 [20]. $\mathbf{M}^{\delta\boldsymbol{\alpha}^c}_{\delta\boldsymbol{\alpha}}$ is provided in the Appendix in Equation 68.

Using this methodology, a state transition matrix including differential SRP for the EROE is computed as

$$\boldsymbol{\Phi}_{srp} = \mathbf{I}_{7\times7} + \gamma_{srp}\sqrt{a}\begin{bmatrix} & 0 \\ & -(\eta+3/\eta)[\mathcal{A}e_x + \mathcal{B}e_y]t \\ & -\frac{1}{\eta}[\mathcal{B}(\eta^2+3e_y^2) + 3\mathcal{A}e_x e_y]t \\ \mathbf{0}_{7\times6} & \frac{1}{\eta}[\mathcal{A}(\eta^2+3e_x^2) + 3\mathcal{B}e_x e_y]t \\ & \mathcal{C}\eta e_x t \\ & \mathcal{C}\eta e_y t \\ & 0 \end{bmatrix} \tag{39}$$

Equation 39 demonstrates a more symmetric structure than 36, primarily due to the intrinsic geometric properties of the EROEs in eccentric orbits. This STM can be included with the J2 STM in Equation 67 to provide a more accurate closed-form model. However, care must be taken when using Equation 39 to propagate for long time periods, especially when including other perturbations. For example, take the example of a high eccentricity orbit with a low altitude periapsis pass. The SRP STM will be accurate at apogee when J2 effects are small. However, the perigee pass may cause a significant change in ω. Since Equation 39 assumes fixed chief orbit elements, this scenario would violate the conditions under which this STM was derived. In such an orbit, the STM would likely need to be reinitialized after each periapsis pass such that chief orbit elements stay updated. Even in the case of no other perturbations, this STM also assumes constant Sun position, and therefore will need to be reinitialized every few days to keep the Sun's orbit elements accurate. Despite these limitations, Equation 39 is an effective tool over moderate time periods where strong perturbations like J2 are not present.

Third-body Perturbations

Third body perturbations are also of interest in HEO, where gravitational perturbations of the Sun and Moon can become significant over an orbit period. Cook provides the derivation for the nonlinear ODE of mean orbit elements subject to perturbations from a third body in a circular orbit about a central body [28]:

$$\begin{bmatrix}\dot{a}\\ \dot{e}\\ \dot{i}\\ \dot{\Omega}\\ \dot{\omega}\\ \dot{M}\end{bmatrix} = \frac{K}{n}\begin{bmatrix} 0 \\ \frac{15}{2}\eta e[\mathcal{A}\mathcal{B}\cos(2\omega) - \frac{1}{2}(\mathcal{A}^2 - \mathcal{B}^2)\sin(2\omega)] \\ \frac{3}{4}\frac{\mathcal{C}}{\eta}[\mathcal{A}(2+3e^2+5e^2\cos(2\omega)) + 5\mathcal{B}e^2\sin(2\omega)] \\ \frac{3}{4}\frac{\mathcal{C}}{\eta\sin(i)}[5\mathcal{A}e^2\sin(2\omega) + \mathcal{B}(2+3e^2-5e^2\cos(2\omega))] \\ -\frac{3}{4}\frac{\mathcal{C}\cos(i)}{\eta\sin(i)}[5\mathcal{A}e^2\sin(2\omega) + \mathcal{B}(2+3e^2-5e^2\cos(2\omega))] \\ 0 \end{bmatrix} \tag{40}$$

where $K = \mu_\odot / r_\odot^3$, and $r_\odot$ is the distance of the third body to the central body. Here, $\odot$ represents a parameter regarding the third body, and $\mathcal{A}$, $\mathcal{B}$, and $\mathcal{C}$ are defined in Equation 34. This expression is typically considered sufficiently accurate when the semi-major axis of the orbit does not exceed one tenth of the orbit radius of the third body. For HEO orbits, solar perturbations could use this model, but not lunar perturbations.

From here, Equation 40 can be substituted into the time derivative of Equation 6 to derive the nonlinear expression for the EROE subject to third body perturbations. By applying the chain rule in Equation 27, a plant matrix that includes third body perturbations can be computed for the mean EROE. The resultant expression is too long to include in the

appendices, so only the methodology is described here. Guffanti provides the plant matrix for the ROE in Equation 3 [20]. Assuming time-invariance over the propagation interval, this plant can be transformed into an STM for the EROE by

$$\mathbf{\Phi}_{3bdy} = (\mathbf{M}_{\delta\boldsymbol{\alpha}}^{\delta\boldsymbol{\alpha}^c})^{-1} \exp(\mathbf{A}_{3bdy}^c)\mathbf{M}_{\delta\boldsymbol{\alpha}}^{\delta\boldsymbol{\alpha}^c} \tag{41}$$

Applying Equation 41 yields an analytical expression for $\mathbf{\Phi}_{3bdy}$.

6. SWARM MAINTENANCE

Given the newly derived STMs, the EROE is to be interpreted as mean elements according to averaging theory [29]. Even if the mean relative semi-major axis is null ($\delta a = 0$), the EROE can drift under the influence of perturbations. Therefore, there is a long-term guidance problem where the relative orbits must stay within certain thresholds to meet passive safety requirements. Due to the ability to include perturbations in the STMs for the EROE, the swarm maintenance problem can be addressed in a closed-form manner.

Out-of-Plane Maintenance

An out-of-plane swarm maintenance strategy for the J2-perturbed state transition matrix in Equation 67 is considered due to its long term accuracy. As observed in Figure 7, there is a long periodic change in the phase of $\delta\boldsymbol{e}$, a nonlinear change in δe magnitude, and a secular drift in δi_y. As seen in Equation 12, the minimum out-of-plane separation between two spacecraft is determined by the phase and magnitudes of $\delta\boldsymbol{e}$ and $\delta\boldsymbol{i}$, and therefore both vectors must be controlled to guarantee passive safety.

An out-of-plane swarm maintenance scheme has already been developed and applied for circular orbits [17]. This method uses a lower and upper bound on ψ and δi_y in order to guarantee a minimum separation. The only difference with eccentric orbits is that now δe must be controlled as well, adding one additional constraint to be considered in the swarm maintenance scheme.

With bounds on phase $[\psi_{min}, \psi_{max}]$, magnitude $[\delta e_{min}, \delta e_{max}]$, and δi_y $[\delta i_{y,min}, \delta i_{y,max}]$, control windows can be defined for $\delta\boldsymbol{e}$ and $\delta\boldsymbol{i}$ as depicted in Figure 8.

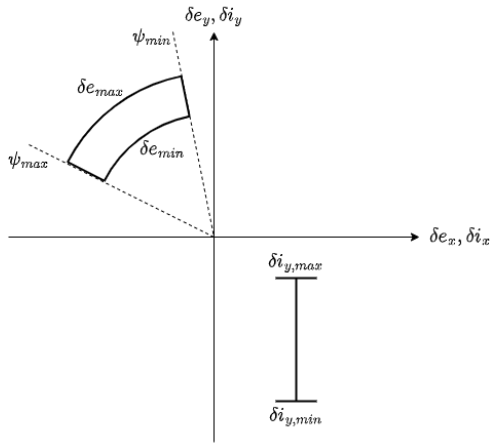

Figure 8: Control Windows for an Out-of-Plane Maintenance Scheme

Maintenance can be performed to keep $\delta\boldsymbol{e}$ and $\delta\boldsymbol{i}$ within the control windows. If $\delta\boldsymbol{e}$ reaches a phase or magnitude boundary, an in-plane maneuver is performed to reset ψ and δe to their minimum and middle ($(\delta e_{min} + \delta e_{max})/2$) values, respectively. The same applies to δi_y. Recall from Equation 12 that a 90° angle between $\delta\boldsymbol{i}$ and $\delta\boldsymbol{e}$ will cause the minimum RN separation to go to zero. In order for these control windows to guarantee a minimum separation, the two vectors must not form a 90° angle at any points within their respective control windows.

As discussed by Lowe and D'Amico for circular orbits, the minimum separation of these control windows lies on one of the boundaries of ψ and δi_y [30]. Therefore, only four checks need to take place in order to compute the minimum separation. The same applies here, because intuitively the separation will be minimized when δe lies on the lower boundary of its control window. Therefore, Algorithm 1 can be used to compute the minimum separation for this swarm maintenance scheme.

Algorithm 1 Computation of Minimum RN Separation

function $(\delta e_{min}, \psi_{min}, \psi_{max}, \delta i_x, \delta i_{y,min}, \delta i_{y,max})$
  for $\psi \in [\psi_{min}, \psi_{max}]$ **do**
    $\delta\boldsymbol{e} \leftarrow$ vector from δe_{min} and ψ
    for $\delta i_y \in [\delta i_{y,min}, \delta i_{y,max}]$ **do**
      $\delta\boldsymbol{i} \leftarrow$ vector from δi_x and δi_y
      $\phi \leftarrow$ compute angle between $\delta\boldsymbol{e}$ and $\delta\boldsymbol{i}$
      $\delta r_{rn} \leftarrow$ Min. Separation, Equation 12
    end for
  end for
  if $\min(\phi) < 90°$ & $\max(\phi) > 90°$ **then**
    $\delta r_{rn}^{min} \leftarrow 0$
  else
    $\delta r_{rn}^{min} \leftarrow \min(\delta r_{rn})$
  end if
  return δr_{rn}^{min}
end function

Maneuver Time Prediction

It is of interest to predict when maneuvers occur without requiring simulation. This can be done semi-analytically by predicting the next maneuver time using the J2 STM, resetting the EROE states to their post-maintenance values at this maneuver time, and repeating. From analysis of the J2 STM, it is possible to predict when maneuvers occur semi-analytically. The time until the next maneuver is the minimum of the times until the different controlled states (δe, ψ, $\delta\lambda$, δi_y) violate their respective control windows. In addition to the $\delta\boldsymbol{e}$ and $\delta\boldsymbol{i}$ bounds discussed in Section 6-A, $\delta\lambda$ will also need to be controlled in most scenarios to prevent along-track drift. The time derivative of $\delta\lambda$ due to J2 perturbations and assuming $\delta a = 0$ is

$$\delta\dot{\lambda} = \frac{\kappa N}{\eta^2}[Ce\delta e_0 \cos(\psi_0 - \omega_0) - \delta i_x \sin(2i)], \tag{42}$$

with the substitutions provided in Equation 67. Using this time derivative, the time until a specified control window is violated and a maneuver is performed can be computed. The same applies to δi_y, where its time derivative is given as

$$\delta\dot{i}_y = -2\kappa[2e\sin(2i)\delta e_0 \cos(\psi_0 - \omega_0) - \delta i_x \sin^2(i)] \tag{43}$$

Once again, this derivative can be used to analytically predict when the next out-of-plane maneuver will occur. δe and ψ

do not have simple derivatives to compute when their control windows are violated. However, bisection can be used to compute these maneuver times. For δe, setting the lower bound of the bisection algorithm to zero seconds, and the upper bound to a sufficiently large number (mission duration, for example), will guarantee convergence to the maneuver time. For ψ, a safe upper bound when accounting for angle wrapping is the time it takes perigee ω to complete one full rotation. Depending on the size of the control window, this can also be decreased to achieve faster convergence.

By predicting the times of future maneuvers and resetting the EROE states to their post-maintenance values, maneuvers times can be predicted over large time horizons. This process is detailed at a high level in Algorithm 2.

Algorithm 2 Computation of Maintenance Maneuver Times

function ($\boldsymbol{\alpha}_0, \delta\boldsymbol{\alpha}_0, t_f$, control windows)
  $t_{curr} = 0$
  times $\leftarrow$ Empty Array
  while $t_{curr} \leq t_f$ **do**
    $t_{prop} \leftarrow \min$(times until control windows violated)
    $\boldsymbol{\alpha} \leftarrow$ Propagate by t_{prop} (Eq. 28)
    $\delta\boldsymbol{\alpha} \leftarrow$ Propagate by t_{prop} (Eq. 67)
    $\delta\boldsymbol{\alpha} \leftarrow$ Reset to post-maneuver values
    times $\leftarrow$ Append with t_{prop}
    $t_{curr} += t_{prop}$
  end while
  return times
end function

This algorithm assumes that the time it takes to complete a maneuver is much smaller than the time between maneuvers. If extra fidelity is needed, content from Section 7 can be used to incorporate maneuver times into t_{prop}, the propagation time.

Passive J2 Perturbation Removal

As discussed in Section 5-A, the additional modes of motion under J2 pose a swarm maintenance problem. While the Section 6-A offers a method to maintain such drift through the use of control windows, another option is to fundamentally design the formation as to remove some of these modes. For J2, there are two formation design constraints that achieve this. Both are derived by inspection of the J2 STM in Equation 67.

The first constraint is given as

$$e(3\cos^2(i) - 1)[\delta e_x \cos(\omega) + \delta e_y \sin(\omega)] = \delta i_x \sin(2i), \tag{44}$$

which is equivalent to

$$e(3\cos^2(i) - 1)\delta e \cos(\omega - \psi) = \delta i_x \sin(2i) \tag{45}$$

If Equations 44 and 45 are satisfied, then mean $\delta\lambda$ and δe magnitude remain constant under J2. This removes two of the four modes and hence is a major simplification of the swarm maintenance problem in eccentric orbits. In circular orbits, designers would typically set $\delta i_x = 0$ in order to remove modes of motion in δi_y and $\delta\lambda$. However, this constraint reveals that a nonzero δi_x can be utilized to simplify relative motion in eccentric orbits.

The second constraint is given as

$$4e[\delta e_x \cos(\omega) + \delta e_y \sin(\omega)] = \delta i_x \tan(i), \tag{46}$$

which is equivalent to

$$4e\delta e \cos(\omega - \psi) = \delta i_x \tan(i) \tag{47}$$

Satisfying Equations 46 and 47 makes δi_y constant under J2. This condition allows the relative inclination vector to be fixed, such that the other EROE can be designed around a fixed point rather than a moving point. The two constraints provided in this section cannot be met simultaneously.

At small separations, these constraints can be scaled to large swarms. Let $\delta\boldsymbol{\alpha}_k$ and $\delta\boldsymbol{\alpha}_j$ be the EROE of a deputy spacecraft k and j with respect to the chief, respectively. Also let $\delta\boldsymbol{\alpha}_{jk} = \delta\boldsymbol{\alpha}_j - \delta\boldsymbol{\alpha}_k$ be the EROE of a deputy spacecraft j with respect to deputy spacecraft k. If both $\delta\boldsymbol{\alpha}_k$ and $\delta\boldsymbol{\alpha}_j$ are chosen such that Equation 45 is valid, then $\delta\dot{\lambda}_k$ and $\delta\dot{\lambda}_j$ both equal zero. Since $\delta\lambda_{jk} = \delta\lambda_j - \delta\lambda_k$, by definition $\delta\dot{\lambda}_{jk}$ must also be zero. This logic is only valid under a first order approximation, and can be applied to any perturbation removal strategy with any ROE definition. This is a convenient property of Relative Orbit Elements that enables rapid scaling of missions from binary formations to large swarms.

7. Impulsive Control of the EROEs

This section details the derivation of a control input matrix for the EROEs in order to model the effects of an impulsive maneuver, i.e. a maneuver modeled as a discontinuity of the velocity at constant position. In addition, it provides a description of a useful closed-loop control policy derived from reachable set theory to optimize maneuver locations and magnitudes with respect to Δv.

Control Input Matrix

A small EROE discontinuity can be computed as a function of a velocity discontinuity in the first order as

$$\Delta\delta\boldsymbol{\alpha} = \Gamma(\boldsymbol{\alpha})\Delta\boldsymbol{v}_{RTN}, \tag{48}$$

where $\Delta\boldsymbol{v}_{RTN} = [\Delta v_R, \Delta v_T, \Delta v_N]^T$ is a small change in velocity expressed in the RTN frame. $\Gamma(\boldsymbol{\alpha})$ can be computed by inverting the Yamanaka-Ankersen STM in Equation 65 and setting the relative position to zero, which yields

$$\Gamma(\boldsymbol{\alpha}) = \frac{\eta}{na}\begin{bmatrix} 2e\sin(\nu) & 2k & 0 \\ \frac{(k+1)(k-2)}{k} & \frac{-e\sin(\nu)(1+k)}{k} & 0 \\ \frac{k\sin(\theta)-2e_y}{k} & \frac{(k+1)\cos(\theta)+e_x}{k} & 0 \\ -\frac{k\cos(\theta)-2e_x}{k} & \frac{(k+1)\sin(\theta)+e_y}{k} & 0 \\ 0 & 0 & \frac{\eta^2\cos(\theta)}{k} \\ 0 & 0 & \frac{\eta^2\sin(\theta)}{k} \end{bmatrix}, \tag{49}$$

A significant feature of Γ is the decoupling between in-plane and out-of-plane control. Δv_N maneuvers will not affect in-plane motion, and $[\Delta v_R, \Delta v_T]^T$ maneuvers will not affect out-of-plane motion. This structure greatly simplifies relative orbit control, as $\delta\boldsymbol{i}$ can be controlled separately from the other EROE. Note that Γ, which is also valid for the quasi-nonsingular EROE definition in Equation 66, reduces to Equation 5 at zero eccentricity.

Closed-Form Impulsive Control using Reachable Set Theory

Reachable set theory can be used to analytically compute optimal maneuver locations, magnitudes, and directions for an arbitrary reconfiguration subject to linear time-variant dynamics. This methodology has been applied by Chernick and D'Amico for spacecraft impulsive relative motion control, and analytical maneuver locations have been discovered [31]. Chernick uses a unique set of relative orbit elements, $\delta\boldsymbol{\alpha}'$, which are defined as

$$\delta\boldsymbol{\alpha}' = \begin{bmatrix} \delta a' \\ \delta\lambda' \\ \delta e'_x \\ \delta e'_y \\ \delta i'_x \\ \delta i'_y \end{bmatrix} = \begin{bmatrix} (a_d - a)/a \\ M_d - M + \eta[\omega_d - \omega + (\Omega_d - \Omega)\cos(i)] \\ e_d - e \\ \omega_d - \omega + (\Omega_d - \Omega)\cos(i) \\ i_d - i \\ (\Omega_d - \Omega)\sin(i) \end{bmatrix} \tag{50}$$

An important property of $\delta\boldsymbol{\alpha}'$ is that mean anomaly only appears in the definition of $\delta\lambda'$, rather than appearing in $\delta\lambda$, δe_x, and δe_y for the EROE. This makes the derivation of closed-form solutions for optimal impulsive control significantly easier; however, this advantage comes at the expense of geometry. $\delta\boldsymbol{\alpha}'$ does not share a first order equivalence with the IC of Yamanaka-Ankersen, and therefore lacks a simple geometric map to relative position and velocity. Nevertheless, $\delta\boldsymbol{\alpha}'$ is an important definition for spacecraft swarms, as closed-form optimal maneuver locations have been derived for this ROE.

Since swarm reconfigurations are generally driven by relative position and velocity requirements, changes in states would generally be defined in terms of $\delta\boldsymbol{\alpha}$ rather than $\delta\boldsymbol{\alpha}'$. The use of reachable set theory can be applied directly to $\delta\boldsymbol{\alpha}$ and is an active area of research. This paper proposes a hybrid approach, where a pseudostate $\Delta\delta\boldsymbol{\alpha}$ is mapped into its corresponding pseudostate $\Delta\delta\boldsymbol{\alpha}'$ to find maneuver locations, magnitudes, and directions. The first-order map between these two pseudostates is

$$\Delta\delta\boldsymbol{\alpha}' = \mathbf{M}_{\delta\boldsymbol{\alpha}}^{\delta\boldsymbol{\alpha}'}\Delta\delta\boldsymbol{\alpha}$$

$$\mathbf{M}_{\delta\boldsymbol{\alpha}}^{\delta\boldsymbol{\alpha}'} = \begin{bmatrix} \frac{1}{\eta^2} & 0 & 0 & 0 & 0 & 0 \\ 0 & \frac{1}{\eta} & -\frac{e_y}{\eta} & \frac{e_x}{\eta} & 0 & 0 \\ 0 & 0 & \cos(\omega) & \sin(\omega) & 0 & 0 \\ 0 & \frac{1}{\eta^2} & -\frac{\sin(\omega)}{e\eta^2} & \frac{\cos(\omega)}{e\eta^2} & 0 & 0 \\ 0 & 0 & 0 & 0 & \frac{1}{\eta^2} & 0 \\ 0 & 0 & 0 & 0 & 0 & \frac{1}{\eta^2} \end{bmatrix} \tag{51}$$

Once $\Delta\delta\boldsymbol{\alpha}'$ is computed, the closed-form solutions available in literature can be used to define the maneuver locations, magnitudes, and directions. Reachable set theory is described in detail by Chernick [31]. This paper will only discuss the algorithms needed to create a maneuver definition.

Three-Burn In-Plane Maneuver Scheme

The three-burn impulsive maneuver scheme is used for an arbitrary in-plane reconfiguration. When only considering Keplerian motion, $\delta\boldsymbol{e}'$ is constant, and the phase of the pseudostate $\Delta\delta\boldsymbol{e}'$ will not be affected by the STM. Therefore, if the maneuver locations are chosen such that the three burns have the same phase as the commanded phase of the pseudostate $\Delta\delta\boldsymbol{e}'$, completion of $\Delta\delta e_x$ will guarantee completion of $\Delta\delta e_y$. Therefore, the number of in-plane pseudostates that need to be controlled is reduced from four to three, enabling a three-burn maneuver scheme.

Investigation of the structure of $\mathbf{M}_{\delta\boldsymbol{\alpha}}^{\delta\boldsymbol{\alpha}'}$ reveals that when mapping from $\Delta\delta\boldsymbol{e}$ to $\Delta\delta\boldsymbol{e}'$, every in-plane reconfiguration case will be $\delta\boldsymbol{e}'$ dominant. Refer to Chernick's work on a discussion of dominance cases; essentially, the psuedostate $\Delta\delta\boldsymbol{e}'$ will always drive the reconfiguration cost, even in cases of large $\Delta\delta\lambda$. Therefore, the three-burn scheme is an appropriate choice, as three pseudostates need to be controlled.

The control input matrix for $\Delta\delta\boldsymbol{\alpha}'$ is given as

$$\Gamma'(\boldsymbol{\alpha}) = \frac{1}{na}\begin{bmatrix} \frac{2}{\eta}e\sin(\nu) & \frac{2}{\eta}k & 0 \\ -\frac{2\eta^2}{k} & 0 & 0 \\ \eta\sin(\nu) & \eta\frac{e+\cos(\nu)(1+k)}{k} & 0 \\ -\frac{\eta}{e}\cos(\nu) & \frac{\eta}{e}\sin(\nu)\frac{1+k}{k} & 0 \\ 0 & 0 & \eta\frac{\cos(\theta)}{k} \\ 0 & 0 & \eta\frac{\sin(\theta)}{k} \end{bmatrix} \tag{52}$$

For simplicity, the scheme described here will only consider tangential maneuvers. Such maneuvers do not reach the true minimum Δv, but are sufficiently close for most applications. Refer to Chernick's work on implementation of a maneuver scheme including radial (Δv_R) and tangential (Δv_T) components.

First, the maneuver locations $\nu_{opt,1}$ and $\nu_{opt,2}$ that achieves the desired pseudostate phase angle of $\delta\boldsymbol{e}$ must be computed. The zeros of the function h are such locations, where h is

$$h(\nu) = a\Delta\delta e'_y(\nu) - \frac{\Delta\delta e'_{y,des}}{\Delta\delta e'_{x,des}} a\Delta\delta e'_x(\nu) \tag{53}$$

where $\Delta\delta e'_y(\nu)$ and $\Delta\delta e'_x(\nu)$ are the effects of a tangential maneuver given in Equation 52. For such maneuvers, analytical maneuver schemes are available [31]. However, the bisection method using appropriate bounds on the optimal maneuver locations provides a more elegant computation method. The ranges of ν_{opt} which guarantee convergence are provided in Table 1.

Table 1: Boundaries of range guaranteeing convergence to the values of ν that are aligned with $\Delta\delta\boldsymbol{e}$.

Condition	$\nu_{opt,1}$ **range**	$\nu_{opt,2}$ **range**
sign($\Delta\delta e'_{x,des}\Delta\delta e'_{y,des}$) = 1	$[\pi, 2\pi]$	$[0, \pi]$
sign($\Delta\delta e'_{x,des}\Delta\delta e'_{y,des}$) = -1	$[0, \pi]$	$[\pi, 2\pi]$

Once bisection is performed and $\nu_{opt,1}$ and $\nu_{opt,2}$ are found, a set of candidate maneuver locations ν_{opt} can be constructed as

$$\nu_{opt} = [\nu_{opt,1}, \nu_{opt,2}, \nu_{opt,1} + 2\pi, ...] \tag{54}$$

until reaching the final possible maneuver location allowed within a specified maximum reconfiguration duration t_f. Using three of these maneuver locations, a linear system can be set up to solve for $\Delta\boldsymbol{v}_T$, the vector of tangential maneuvers used to compute the reconfiguration. This system is given as

$$\begin{bmatrix} \Delta\delta a' \\ \Delta\delta\lambda' \\ \Delta\delta e'_x \end{bmatrix} = \sum_{i=1}^{3} \Phi'(t_f, t_i)\Gamma'(\nu_i(t_i))\Delta v_{T,i}, \tag{55}$$

where t_i is the time at maneuver location ν_i, and Φ' is the Keplerian STM for $\delta\boldsymbol{\alpha}'$, which is

$$\Phi'(t_f, t_i) = \begin{bmatrix} 0 \\ -\frac{3}{2}n(t_f - t_i) \quad \mathbf{0}_{6\times5} \\ \mathbf{0}_{4\times1} \end{bmatrix} + \mathbf{I}_{6\times6} \tag{56}$$

Note that $\Delta\delta e_y$ is not included in Equation 55; this is because the maneuver locations are selected such that they are aligned with the phase of $\Delta\delta\boldsymbol{e}$. Therefore, completion of $\Delta\delta e_x$ will also guarantee that $\Delta\delta e_y$ is fulfilled. For the case of $\Delta\delta e_x = 0$, switching the third row to use nonzero $\Delta\delta e_y$ typically yields more numerically stable results.

From here, combinations of maneuver locations can be iterated through until the lowest Δv solution is found, as described in Algorithm 3.

Algorithm 3 Closed-form maneuver scheme solution.

function RECONFIG($\boldsymbol{\alpha}_0, \delta\boldsymbol{\alpha}_0, \delta\boldsymbol{\alpha}_f, \Delta t_f$)
  $\nu_{opt}(t_{opt}) \leftarrow$ Find optimal maneuver locations (Eq. 53)
  combos = nchoosek(len(ν_{opt}),3)
  for combo$_k$ in combos **do**
    $\mathbf{A}_k \leftarrow$ Form linear system (Eq. 55)
    $\Delta\boldsymbol{v}_T = \mathbf{A}_k^{-1}[\Delta\delta a', \Delta\delta\lambda', \Delta\delta e_x']^T$
    if $||\Delta\boldsymbol{v}_T||_1 \leq \boldsymbol{v}_{T,best}$ **then**
      combo$_{best}$ = combo$_i$
      $\Delta\boldsymbol{v}_{T,best} = \Delta\boldsymbol{v}_T$
    end if
  end for
  return $\boldsymbol{v}_{T,best}$, combo$_{best}$
end function

Algorithm 3 also provides the three maneuver vectors for a reconfiguration. From here, the total Δv for a maneuver scheme can be computed by summing over the L2 norms of these three vectors.

One-Burn Out-of-Plane Maneuver Scheme

Out-of-plane control is a much simpler problem, because $\delta\boldsymbol{i}$ does not move under Keplerian dynamics. Therefore, as long as the maneuver location is aligned with the pseudostate phase, the maneuver can be completed in one burn.

From inspection of Equation 52, the maneuver location can be computed as

$$\theta = \omega + \nu = \arctan\left(\frac{\Delta\delta i'_{y,des}}{\Delta\delta i'_{x,des}}\right) \tag{57}$$

In addition, the total Δv required to complete an out-of-plane maneuver is a function of the pseudostate $\Delta\delta i'$ magnitude as

$$|\Delta v_N| = \frac{nak}{\eta}\Delta\delta i' \tag{58}$$

Substituting Equation 57 into k in Equation 58 yields the Δv required to complete an out-of-plane maneuver.

8. MARS GRAVITY EXPERIMENT

Validation of the closed-form models and control laws is performed through the development of a conceptual spacecraft swarm mission denoted the Mars Gravity Experiment. The mission objective is to collect high-resolution gradiometry data by measuring the range, range-rate, and accelerations between multiple spacecraft at low altitudes [32]. This measurement strategy is similar to the GRACE [11] and GRAIL [33] missions, which recovered the gravity field of the Earth and Moon to unprecedented accuracy, respectively. However, a third spacecraft is added for this mission design as to enable gravity gradient measurements in multiple directions simultaneously.

This section will detail the design of the absolute orbit of the chief, and the relative orbits of the two deputies. Problems of swarm maintenance and Δv budgeting are addressed in closed-form using the content of Sections 6 and 7. Simulation results and analysis are provided in Section 9.

Chief Orbit Design

The design of the chief orbit is subject to several considerations. First, the measurement altitude must be placed as low as possible to maximize sensitivity to the gravitational force. However, the use of a circular orbit would shorten the life of the mission due to atmospheric drag. An eccentric orbit with measurements being taken during periapsis pass is instead used, as the orbit need to circularize prior to altitude decay. Given design heritage for aerobraking missions [34], an altitude of 170 km is above the range where significant atmospheric effects are present. However, decreasing measurement altitude from 170 km to 130 km yields over a 70% increase in gravity gradient resolution, so periapsis will be placed at 130 km with the understanding that periodic apogee boosting will have to occur to maintain the orbit.

Since scientific measurements can only be taken during periapsis passes, J2 perturbations will be leveraged in order to move the periapsis location ω. This enables comprehensive scanning of the surface depending on the inclination. Another operational constraint is power, as it is important to ensure that apoapsis never resides in the shadow of mars. In order to guarantee access to the sun, the mission is placed in a Sun-Synchronous Orbit (SSO) where $\dot{\Omega} = 0.524^\circ/\text{day}$. Given the perigee altitude and ascending node precession rate constraints, there is a unique inclination and periapsis precession rate for each eccentricity. In order to ensure high scanning latitudes for sufficient Mars ground coverage, the inclination must be less than 105°. Given this, an eccentricity of 0.4 was selected to provide a reasonable tradeoff between apoapsis altitude and keeping the periapsis rate sufficiently high, at about $1.2^\circ/\text{day}$.

Using this orbit design, the initial mean chief orbit elements are given in Table 2.

Table 2: Chief Mean Initial Orbit Elements

Orbit Element	Value
Semi-Major Axis (a)	5866 km
Eccentricity (e)	0.4
Inclination (i)	99.5°
Longitude of Ascending Node (Ω_0)	75°
Argument of Perigee (ω_0)	188°

ω_0 is chosen arbitrarily. Ω_0 is chosen such that the orbit angular momentum is closely aligned with the initial sun vector. Since this is a Sun-Synchronous orbit, this ensures that as ω drifts, the three spacecraft always have line of sight to the sun. A visualization of this orbit is provided in Figure 9.

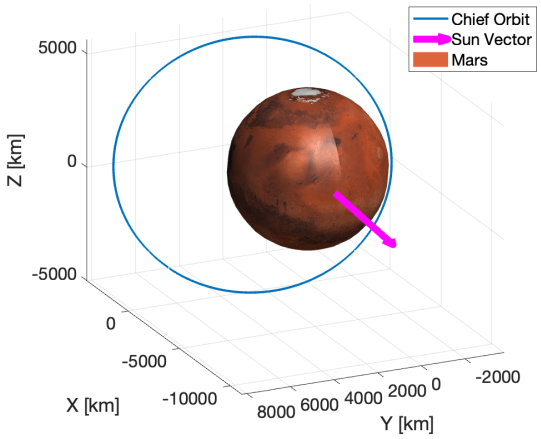

Figure 9: Chief initial orbit.

Relative Orbit Design

The use of three spacecraft allows for gravity gradient measurements to be taken in multiple directions simultaneously. In addition, by investigation of Equation 9, perigee precession can be used to dynamically adjust the baselines for geometric dilution of precision. Deputy 1 will primarily be responsible for measurements in the chief's orbit plane, and Deputy 2 will be responsible for measurements in the cross-track direction. In terms of EROE, Deputy 1 will have a large δe and small δi, while Deputy 2 will have a large δi with a small δe. Passive safety will be guaranteed by a minimum separation in the RN plane using methods discussed in Sections 4-A and 4-C.

First, the locations of the two deputies at periapsis are constrained such that the inter-spacecraft range is bounded. By substituting $\nu = 0$ into Equation 9 and setting δa and $\delta\lambda$ to zero, the relative position between deputies and chief at periapsis is given by

$$\begin{aligned} \frac{x}{a} &= -\delta e \cos(\omega - \psi) \\ \frac{y}{a} &= \frac{2+e}{1+e}\delta e \sin(\omega - \psi) \\ \frac{z}{a} &= \frac{1}{1+e}\delta i \sin(\omega - \phi) \end{aligned} \tag{59}$$

Equation 59 can be used for deputy placement at periapsis. Next, Equation 20 can be modified as

$$\begin{aligned} \delta e_{min} &\geq \beta\frac{\epsilon}{a} \\ \delta i_{min} &\geq \beta\frac{\epsilon}{a}(1+e) \end{aligned} \tag{60}$$

In order for Equation 20 top be valid, ψ and ϕ must be equal or separated by $180°$. β is a safety factor to ensure deviations in the phases ψ and ϕ do not cause a minimum separation violation. The minimum separation ϵ is set to 500 meters for this design, and β is set to 1.1.

First, the relative orbit of Deputy 1 is designed. This spacecraft is designed to have a maximum of 10 km separation in the along-track direction for scientific measurements at periapsis. Since ω rotates, it makes sense to consider the extreme where $\sin(\omega - \psi) = 1$. From Equation 59, this can be written as

$$\frac{y_{max}}{a} = \frac{2+e}{1+e}\delta e, \tag{61}$$

where y_{max} is the maximum along-track separation. δe can be computed from this equation, with the assumption that $\delta e > \delta e_{min}$. δi is set to δi_{min} from Equation 60 as to ensure Deputy 1 is passively safe. All that remains is to select the phases ψ and ϕ. From inspection of the J2 STM in Equation 67, the term $\Phi_{6,5}$ is highly perturbative on δi_y in near-polar orbits. Therefore, ϕ is set to $270°$ such that δi_x is zero, minimizing this unwanted J2 effect. This requires that ψ be $90°$. Next, the relative orbit of Deputy 2 is designed. This spacecraft is designed to have a maximum of 5 km separation in the cross-track direction for measurements at periapsis. From Equation 59, this can be written as

$$\frac{z_{max}}{a} = \frac{1}{1+e}\delta i, \tag{62}$$

where z_{max} is the maximum cross-track separation. δi can be computed from this equation, assuming $\delta i > \delta i_{min}$. δe is set to δe_{min} as to enforce passive safety in the RN plane. In addition, $\delta \boldsymbol{e}$ and $\delta \boldsymbol{i}$ are set to be anti-parallel to Deputy 1 as to maximize separation between the two deputies. As seen from Equation 19, RN passive safety for the entire swarm is guaranteed even if the phases were aligned. From this design methodology, the nominal EROEs for the deputies are given in Table 3 and visualized in Figure 10.

Table 3: Deputy EROEs

EROE $a\delta\boldsymbol{\alpha}$	**Deputy 1**	**Deputy 2**
$a\delta a$	0 km	0 km
$a\delta\lambda$	0 km	0 km
$a\delta e_x$	0 km	0 km
$a\delta e_y$	5.83 km	-0.55 km
$a\delta i_x$	0 km	0 km
$a\delta i_y$	-0.77 km	7.0 km

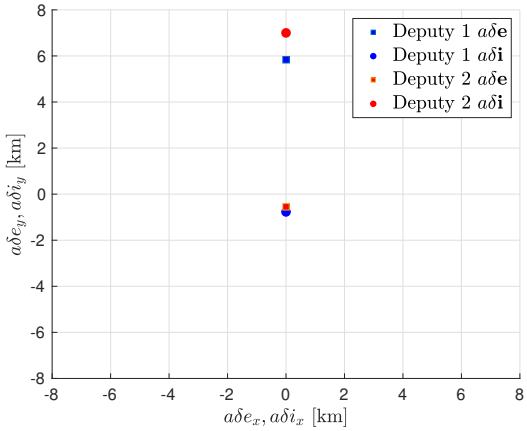

Figure 10: Nominal EROE for the two deputies with respect to the chief.

As discussed, the swarm geometry changes as ω rotates, which enables measurements to be taken across a number of directions. One example geometry is provided in Figures 11 and 12 for $\omega = 180°$.

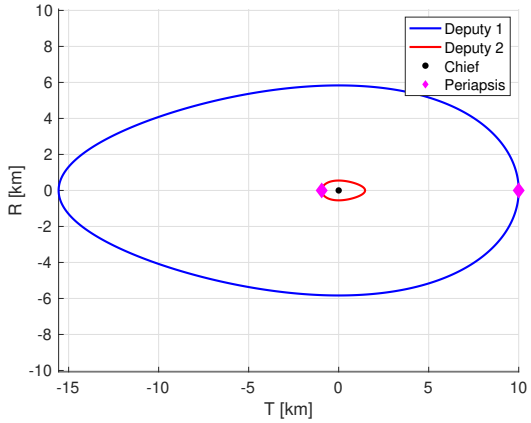

Figure 11: In-plane relative position of the two deputies with respect to the chief for $\omega = 180°$.

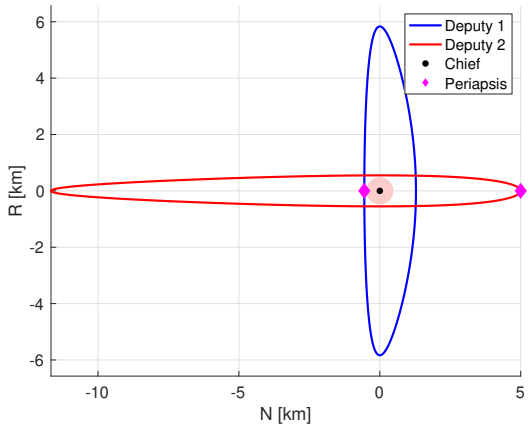

Figure 12: Out-of-plane relative position of the two deputies with respect to the chief for $\omega = 180°$.

As seen in Figure 12, a minimum separation of 500 meters is guaranteed for $\omega = 180°$. The true minimum separation against the analytical lower bound from Equation 12 is provided in Figure 13 against varying ω.

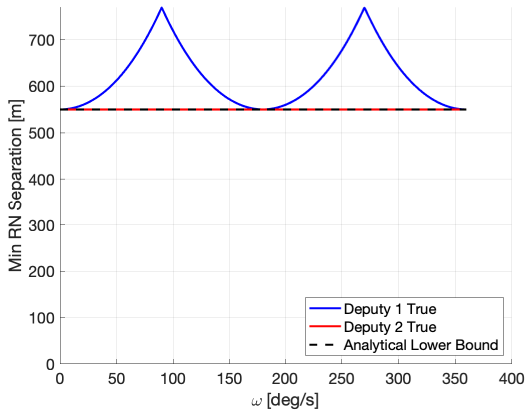

Figure 13: True minimum separation against the analytical lower bound.

As can be observed, the distance of Deputy 2 is tight against the analytical lower bound. This is because the minimum RN separation is guaranteed entirely by a radial separation with no normal component, as seen in Figure 12. Since radial separation is not affected by the value of k (see Equation 9, the lower bound in this case is tight for all ω. This is not true for Deputy 1. Finally, it is of interest to investigate the distribution of deputy locations during periapsis across all possible values of ω. This can be done using Equation 59 and the periapsis locations are provided in Figure 14.

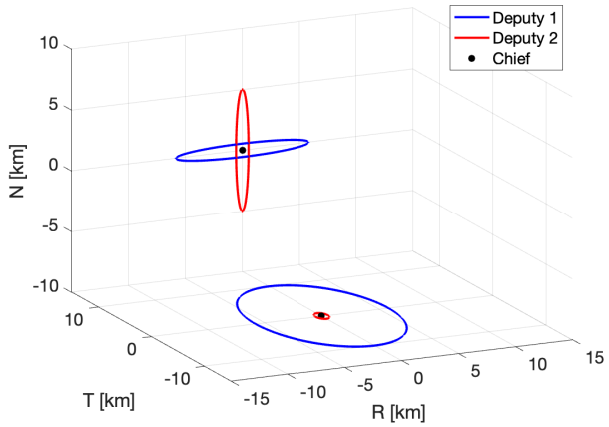

Figure 14: Deputy periapsis locations projected onto the RT and RN planes, plotted for all ω.

As expected, the periapsis locations for Deputy 1 mostly reside in the RT plane, with a small N component for passive safety. The converse is true for Deputy 2.

Swarm Maintenance—In this section, a swarm maintenance scheme is designed for Deputy 1 considering J2 perturbations. The control windows used in this design are provided in Table 4.

Table 4: Deputy 1 Control Windows

EROE	Min	Max
$a\delta\lambda$	-1 km	1 km
$a\delta e$	5.83 km	6.42 km
ψ	80°	100°
$a\delta i_y$	-1.54 km	-0.77 km

The minimum δe is set to the nominal value from Table 3, and the magnitude is allowed to exceed this nominal value by 10%. The phase of $\delta \boldsymbol{e}$ has a nominal value of 90° and is allowed to fluctuate ±10°. When either of these windows is violated, a maneuver is performed to drive δe back to its middle value ($(\delta e_{min} + \delta e_{max})/2$), and maximum phase because $\dot{\psi} < 0$. To guarantee a minimum separation in the RN plane, the smallest magnitude of δi_y is set to its nominal value in Table 3. The maximum value is set to twice that value as to disallow a large cross-track separation, and $\delta\lambda$ is allowed to fluctuate within ±1 km.

In order to ensure passive safety across the entire control window, Algorithm 1 can be used to verify a minimum separation in the RN plane. For Deputy 1, the computed value is 541.6 meters. This is above the minimum separation threshold ϵ of 500 meters due to the applied safety factor β. The importance of this safety factor is apparent here, as setting $\beta = 1$ would have yielded a minimum separation less than 500 meters.

Delta-V Budgeting—By combining Algorithm 2 which predicts maneuver times with Algorithm 3 which can provide Δv for a maneuver, long term Δv budgeting can be performed. At each computed maneuver time, the in-plane and out-of-plane maneuver schemes can be used to find the Δv required to drive the EROE back inside the control windows. This process can be extended over large time horizons to get fuel estimates for different swarm designs at low computational cost. Using the control windows described in Table 4, Δv budgeting was performed for Deputy 1. The estimated accumulated Δv over a 70 day time period is provided in Figure 18, which compares these results against high-fidelity nonlinear simulation (see Section 9-B).

9. Simulation and Results

In order to assess the performance of the closed-form models and control schemes provided in this paper, high-fidelity numerical simulations are run for the Mars Gravity Experiment mission design. This section will detail the parameters of the linear model and the numerical simulation, and provide results and analysis of the performance of the closed-loop modeling and control strategies provided in this paper.

Linear Relative Orbit Model

The linear relative orbit simulation utilizes the STMs developed in Section 5 to propagate the mean EROE directly. The STMs are initialized with the initial chief and sun orbit elements, and propagated for different final times t. This model is defined as

$$\delta\boldsymbol{\alpha}(t) = [\Phi_{J2+kep}(t) + \Phi_{srp,1:6}(t)] \begin{bmatrix} \delta\boldsymbol{\alpha}_0 \\ \Delta B_{srp} \end{bmatrix} \tag{63}$$

where $\Phi_{srp,1:6}$ is the first six rows of Φ_{srp}, as this model assumes constant differential SRP ballistic coefficient.

Nonlinear Orbit Simulation

The nonlinear orbit simulation operates by propagating position and velocity for each spacecraft under the influence of Keplerian dynamics and perturbations numerically using the fundamental orbital differential equations. Such a simulation allows for computation of osculating orbit elements to compare against the mean elements from the linear model.

The nonlinear simulation setup is provided in Table 5. The spacecraft properties are provided in Table 6. The initial conditions are provided in Tables 2 and 3.

Modeling Results

Using the simulation setup described in the previous section, the linear model can be compared against the nonlinear simulation. First, Figure 15 compares the osculating EROE of Deputy 1 against the mean predictions from the linear model over 10 orbits.

Table 5: High-Fidelity Orbit Simulation Environment

Simulation Parameter	Model
Numerical Integrator	RK-4
Time Step	6 seconds
Gravity Field	J2 Spherical Harmonic
Third Body	Sun Point Mass
Solar Radiation Pressure	Flat Plate Model Cylindrical Shadow Model
Planetarty/Sun Ephemerides	SPICE (NASA JPL Toolkit)

Table 6: Deputy Simulation Parameters

Parameter	Chief	Deputy 1	Deputy 2
C_r	1.29	1.90	1.90
A_r	3.34 m^2	1.77 m^2	1.77 m^2
m	339 kg	211 kg	211 kg

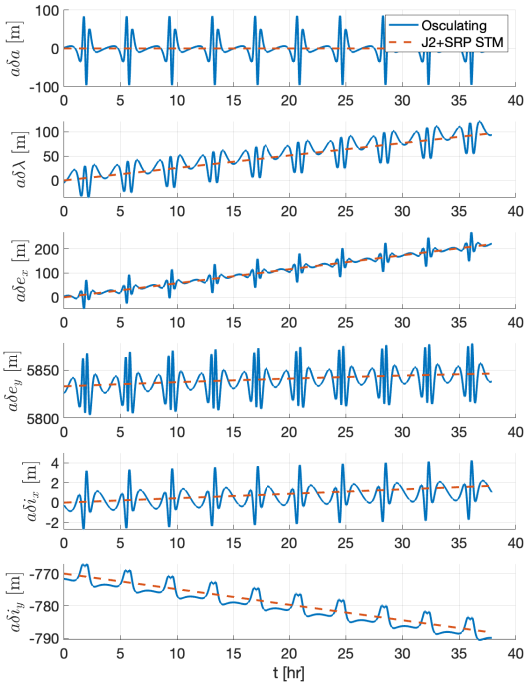

Figure 15: Osculating EROE of Deputy 1 for the nonlinear orbit simulation vs. mean EROE from the linear models.

The EROE from the nonlinear simulation osculate around the predictions from the mean linear simulation. The drift of δe, $\delta\lambda$, and δi_y are dominated by J2 perturbations, while the drift of δi_x is dominated by SRP perturbations. It is worth noting that the passively safe swarm design was done using mean EROE, but the osculating EROE fluctuate around these design parameters. This can lead to a minimum separation violation, but typically $\delta\boldsymbol{r}$ is only marginally affected by osculation. Increasing β slightly in Equation 60 accounts for this. Next, the position estimate from the linear simulation is computed by converting the mean EROE into osculating, then applying the geometric map in Equation 9. The norm error is shown

on a logarithmic scale in Figure 16 for 40 orbits.

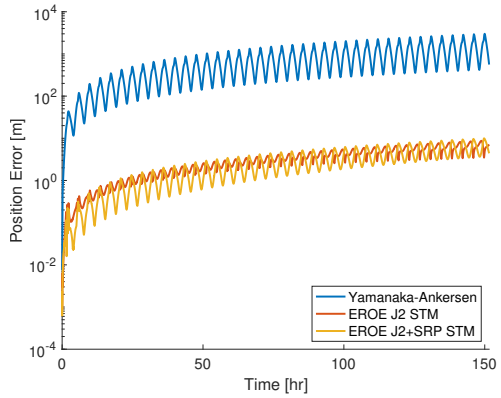

Figure 16: Position error of linear models over 40 orbits.

There is oscillation in the errors, reaching their maximum at apoapsis and minimum at periapsis. The Yamanaka-Ankersen solution is computed using the initial EROEs in place of the integration constants. This slightly improves the accuracy over a Cartesian-based initialization, but it is still outperformed by the EROE STMs as it does not include perturbations. The model including SRP provides modest improvements just including J2, but only for short time periods as the perigee precession eventually invalidates the assumption of contain chief orbit elements.

Swarm Maintenance Control Results

In order to test the accuracy of the closed-form swarm maintenance model, the deputies are equipped with swarm maintenance control algorithms. When the deputy exits a control window, a series of maneuvers are scheduled to drive back to the beginning of the control window according to the three-burn maneuver scheme (Section 7-C) for in-plane maneuvers, and the one-burn scheme (Section 7-D) for out-of-plane maneuvers. No navigation uncertainties are considered.

The closed-form model and numerical simulation are run for 400 orbits. The $\delta\boldsymbol{e}$ and $\delta\boldsymbol{i}$ trajectories are shown in Figure 17.

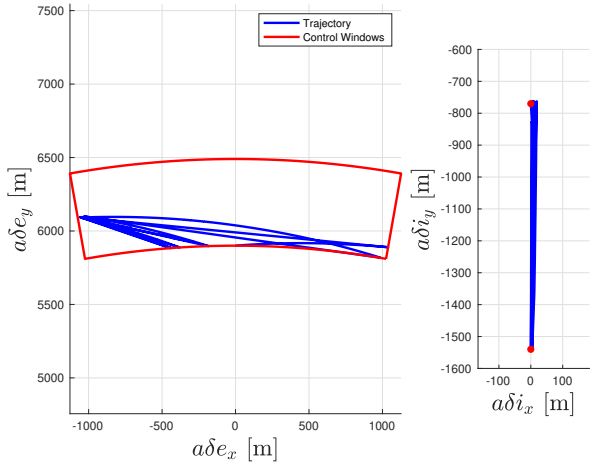

Figure 17: $\delta\boldsymbol{e}$ and $\delta\boldsymbol{i}$ trajectory of Deputy 1 over 400 orbits.

As can be observed, maneuvers are performed such that the trajectory stays within the control windows. The accumulated Δv of Deputy 1 over these maneuvers is given in Figure 18. The closed-form model provides the maneuver times, individual maneuver Δv magnitudes, and accumulated Δv over long time periods with a high level of accuracy. The error statistics for this scenario are provided in Table 7.

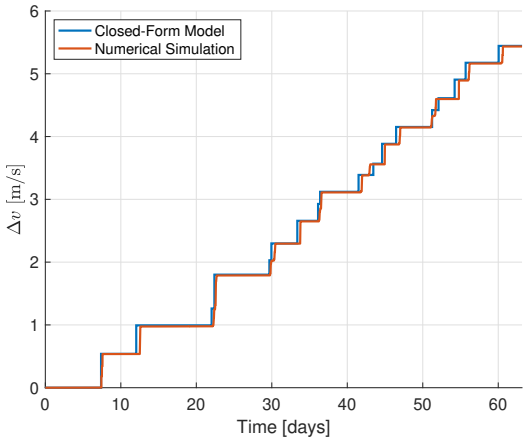

Figure 18: Accumulated Δv estimate from the closed-form model compared against nonlinear simulation.

Table 7: Closed-form swarm maintenance model error statistics

Statistic	**Error Mean**	**Error STD** (1σ)
Accumulated Δv [cm/s]	2.42 (0.5%)	-
Maneuver Δv [cm/s]	0.36 (1.1%)	0.60 (1.8%)
Maneuver Time [hr]	5.5 (0.6%)	2.0 (0.2%)

Running in MATLAB on an M1 Macbook Air with 16 GB of memory, the closed-form algorithm took 28 milliseconds to complete. Such is the advantage of using closed-form models over a full numerical simulation, as different designs can be rapidly iterated through to find the best choice for a particular mission.

Swarm Reconfiguration Results

In order to assess the accuracy of the impulsive control laws, a single maneuver executed in open loop is considered. This is in contrast to the swarm maitenance controller, which incorporates secondary closed-loop algorithms to drive the tracking error to zero. The maneuver definition is provided in Table 8.

Table 8: Reconfiguration Definition for Deputy 1.

EROE	**Initial** $\delta\boldsymbol{\alpha}_0$	**Final** $\delta\boldsymbol{\alpha}_f$	$\Delta\delta\boldsymbol{\alpha}$
$a\delta a$	0 m	0 m	0 m
$a\delta\lambda$	0 m	0 m	0 m
$a\delta e_x$	0 m	-812 m	-812 m
$a\delta e_y$	5833 m	5777 m	-56 m
$a\delta i_x$	0 m	0 m	0 m
$a\delta i_y$	-770 m	0 m	770 m

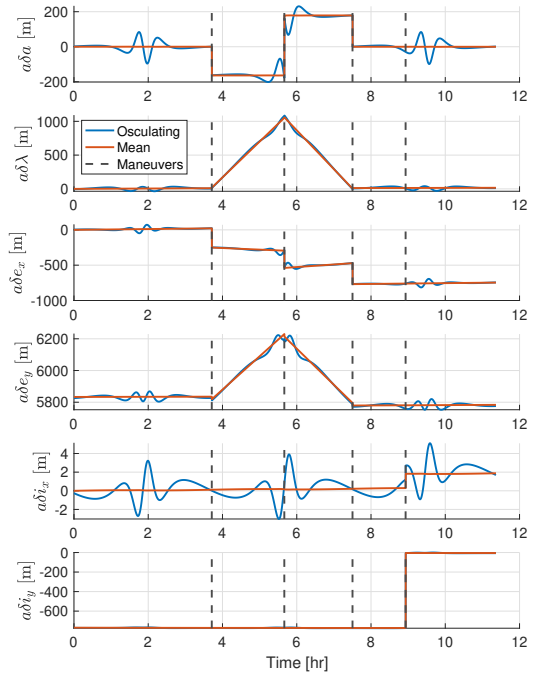

Figure 19: Trajectory of Deputy 1 over the reconfiguration in Table 8.

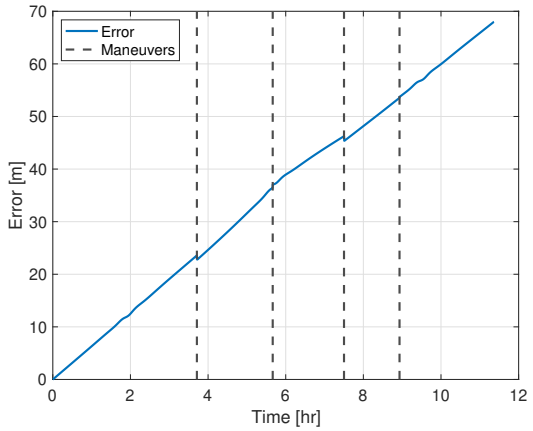

Figure 20: Control tracking error of Deputy 1.

$\delta\boldsymbol{\alpha}_f$ represents the EROE for a different swarm design in which Equation 45 is applied for $\omega_0 = 188°$. This allows δe to remain constant and ensures $\dot{\psi} = \dot{\omega}$. From Equation 9, the in-plane geometry would be constant under J2 in this design, enabling sampling the gravity gradient in the same direction over multiple orbits. This maneuver is executed using the first three maneuver locations for the in-plane maneuver. The out-of-plane maneuver is completed second.

The trajectory that results from performing this reconfiguration is provided in Figure 19. The maneuver lowers δa below zero, which causes an increase in $\delta\lambda$ and δe_x. The second maneuer inverts this drift, and the third maneuver drives δa back to zero. The fourth maneuver completes the $\delta\boldsymbol{i}$ maneuver. The trajectory from this open-loop maneuver will not perfectly conform to the commanded, and the control tracking error, computed as the L2 norm of the difference between true and commanded EROE states, is provided in Figure 20. Although there are small fluctuations in the error due to maneuver execution, the dominant error source is perturbations, which are not accounted for the in the impulsive maneuver scheme. This error, at its peak, is about 6.1% of the L2 norm of the pseudostate command. This percentage is in line with performance expections for an open loop control policy, demonstrating that the analytical maneuver schemes can provide moderately accurate maneuever definitions over a small number of orbits. Longer reconfigurations will have higher error.

10. Conclusions

The use of eccentric orbits for distributed space systems is increasing due to numerous capabilities that such orbits provide over low earth orbit. However, the relative motion dynamics in such orbits are more complex, making problems such as passive safety and relative orbit control more difficult to address in closed-form. Furthermore, the state of the art analytical models for relative motion in eccentric orbits do not consider the effects of differential perturbations on the relative orbit.

This paper introduces a new state representation, denoted the Eccentric Relative Orbit Elements (EROEs), to address these challenges. EROEs enable an intuitive geometrical insight into relative orbits. Expressions for minimum inter-spacecraft separation are provided to guarantee passive safety in closed-form. STMs for the EROEs are derived which include perturbations, improving on the accuracy of STMs based in relative position and velocity coordinates. This enables the design of swarm maintenance strategies in closed-form. Finally, existing closed-form control policies based on reachable set theory are applied to the EROEs. Combining this control policy with a chosen swarm maintenance scheme enables semi-analytical Δv budgeting.

The closed-form models and algorithms proposed in this paper are applied to the swarm design of a Mars gradiometry mission. Passive safety, swarm maintenance, and Δv budgeting are all addressed in closed form through this design process. Comparing with nonlinear simulation, the STMs demonstrate improved accuracy over the Yamanaka-Ankersen STM and the analytical maneuver times and magnitudes closely match the true swarm behavior.

Future work includes the direct application of reachable set theory to the EROEs, which will likely simplify the analytical maneuver scheme. Derivation of an STM including differential drag is a logical next step, as well as a third-body STM that is applicable for lunar perturbations in high eccentricity orbits.

Appendices

Clohessy-Wiltshire State Transition Matrix

The CW STM is given as

$$\begin{bmatrix} x \\ y \\ z \\ \dot{x} \\ \dot{y} \\ \dot{z} \end{bmatrix} = a \begin{bmatrix} 1 & 0 & \Psi_{x,3} & \Psi_{x,4} & 0 & 0 \\ \Psi_{y,1} & 1 & \Psi_{y,3} & \Psi_{y,4} & 0 & 0 \\ 0 & 0 & 0 & 0 & \Psi_{z,5} & \Psi_{z,6} \\ 0 & 0 & \Psi_{\dot{x},3} & \Psi_{\dot{x},4} & 0 & 0 \\ \Psi_{\dot{y},1} & 0 & \Psi_{\dot{y},3} & \Psi_{\dot{x},4} & 0 & 0 \\ 0 & 0 & 0 & 0 & \Psi_{\dot{z},5} & \Psi_{\dot{z},6} \end{bmatrix} \begin{bmatrix} K_1 \\ K_2 \\ K_3 \\ K_4 \\ K_5 \\ K_6 \end{bmatrix} \tag{64}$$

with the following substitutions

$$\Psi_{x,3} = -\cos(u) \quad \Psi_{x,4} = -\sin(u)$$

$$\Psi_{y,1} = -\frac{3}{2}(u-u_0) \quad \Psi_{y,3} = 2\sin(u) \quad \Psi_{y,4} = -2\cos(u)$$
$$\Psi_{z,5} = \sin(u) \quad \Psi_{z,6} = -\cos(u)$$
$$\Psi_{\dot{x},3} = n\sin(u) \quad \Psi_{\dot{x},4} = -n\cos(u)$$
$$\Psi_{y,1} = -\frac{3}{2}n \quad \Psi_{\dot{y},3} = 2n\cos(u) \quad \Psi_{\dot{y},4} = 2n\sin(u)$$
$$\Psi_{\dot{z},5} = n\cos(u) \quad \Psi_{\dot{z},6} = n\sin(u)$$

where $u = u_0 + nt$ is the mean argument of latitude at propagation time t, and $n = \sqrt{\mu/a^3}$ is the mean motion of the chief.

Yamanaka-Ankersen State Transition Matrix

The YA STM can be expressed as

$$\begin{bmatrix} x \\ y \\ z \\ \dot{x} \\ \dot{y} \\ \dot{z} \end{bmatrix} = a \begin{bmatrix} \Psi_{x,1} & 0 & \Psi_{x,3} & \Psi_{x,4} & 0 & 0 \\ \Psi_{y,1} & \Psi_{y,2} & \Psi_{y,3} & \Psi_{y,4} & 0 & 0 \\ 0 & 0 & 0 & 0 & \Psi_{z,5} & \Psi_{z,6} \\ \Psi_{\dot{x},1} & 0 & \Psi_{\dot{x},3} & \Psi_{\dot{x},4} & 0 & 0 \\ \Psi_{\dot{y},1} & \Psi_{\dot{y},2} & \Psi_{\dot{y},3} & \Psi_{\dot{y},4} & 0 & 0 \\ 0 & 0 & 0 & 0 & \Psi_{\dot{z},5} & \Psi_{\dot{z},6} \end{bmatrix} \begin{bmatrix} C_1 \\ C_2 \\ C_3 \\ C_4 \\ C_5 \\ C_6 \end{bmatrix}, \tag{65}$$

with the following substitutions

$$\Psi_{x,1} = \frac{1}{k} - \frac{3}{2}\frac{e}{\eta^3}\sin(\nu)nt \quad \Psi_{x,3} = -\cos(\theta) \quad \Psi_{x,4} = -\sin(\theta)$$
$$\Psi_{y,1} = -\frac{3}{2}\frac{k}{\eta^3}nt \quad \Psi_{y,2} = \frac{1}{k} \quad \Psi_{y,3} = (\frac{1}{k}+1)\sin(\theta)$$
$$\Psi_{y,4} = -(\frac{1}{k}+1)\cos(\theta) \quad \Psi_{z,5} = \frac{1}{k}\sin(\theta) \quad \Psi_{z,6} = -\frac{1}{k}\cos(\theta)$$
$$\Psi_{\dot{x},1} = -\frac{1}{k^2}\dot{k} - \frac{3}{2}\frac{e}{\eta^3}[\dot{\nu}nt\cos(\nu) + n\sin(\nu)] \quad \Psi_{\dot{x},3} = \sin(\theta)\dot{\nu}$$
$$\Psi_{\dot{x},4} = -\cos(\theta)\dot{\nu} \quad \Psi_{\dot{y},1} = -\frac{3}{2}\frac{\dot{k}}{\eta^3}nt - \frac{3}{2}\frac{k}{\eta^3}n \quad \Psi_{\dot{y},2} = -\frac{\dot{k}}{k^2}$$
$$\Psi_{\dot{y},3} = -\frac{\dot{k}}{k^2}\sin(\theta) + (\frac{1}{k}+1)\cos(\theta)\dot{\nu}$$
$$\Psi_{\dot{y},4} = \frac{\dot{k}}{k^2}\cos(\theta) + (\frac{1}{k}+1)\sin(\theta)\dot{\nu}$$
$$\Psi_{\dot{z},5} = -\frac{\dot{k}}{k^2}\sin(\theta) + \frac{1}{k}\cos(\theta)\dot{\nu} \quad \Psi_{\dot{z},6} = \frac{\dot{k}}{k^2}\cos(\theta) + \frac{1}{k}\sin(\theta)\dot{\nu}$$

where $k = 1 + e\cos(\nu)$ and $\dot{k} = -e\sin(\nu)\dot{\nu}$. It is worth noting that all terms that are a function of ν are multiplied by e, and hence do not create a singularity at $e = 0$.

Quasi-nonsingular EROE Definition

The EROE definition in terms of quasi-nonsingular orbit elements is provided as

$$\delta\boldsymbol{\alpha}^* = \begin{bmatrix} \delta a^* \\ \delta\lambda^* \\ \delta e_x^* \\ \delta e_y^* \\ \delta i_x^* \\ \delta i_y^* \end{bmatrix} =$$
$$\begin{bmatrix} \eta^2(a_d - a)/a \\ (1+\frac{1}{\eta^2+\eta})(e_y e_{d,x} - e_x e_{d,y}) + \frac{1}{\eta}(u_d - u) + \eta^2(\Omega_d - \Omega)\cos(i) \\ e_{d,x}(1+\frac{e_y^2}{\eta^2+\eta}) - e_x + \frac{1}{\eta}e_y(u_d - u - \frac{e_{d,y}e_x}{\eta+1}) \\ e_{d,y}(1+\frac{e_x^2}{\eta^2+\eta}) - e_y - \frac{1}{\eta}e_x(u_d - u + \frac{e_{d,x}e_y}{\eta+1}) \\ \eta^2(i_d - i) \\ \eta^2(\Omega_d - \Omega)\sin(i) \end{bmatrix} \tag{66}$$

J2-Perturbed State Transition Matrix

The J2-perturbed STM is given as

$$\boldsymbol{\Phi}_{J2+kep}(t) = \frac{1}{\eta^2}\begin{bmatrix} \eta^2 & 0 & 0 & 0 & 0 & 0 \\ \Phi_{2,1} & \eta^2 & \Phi_{2,3} & \Phi_{2,4} & \Phi_{2,5} & 0 \\ \Phi_{3,1} & 0 & \Phi_{3,3} & \Phi_{3,4} & \Phi_{3,5} & 0 \\ \Phi_{4,1} & 0 & \Phi_{4,3} & \Phi_{4,4} & \Phi_{4,5} & 0 \\ 0 & 0 & 0 & 0 & \eta^2 & 0 \\ \Phi_{6,1} & 0 & \Phi_{6,3} & \Phi_{6,4} & \Phi_{6,5} & \eta^2 \end{bmatrix}, \tag{67}$$

with the following substitutions

$$\Phi_{2,1} = -\frac{t(3n - 7\kappa MC)}{2\eta} \quad \Phi_{2,3} = t\kappa e\cos(\omega_0)NC$$
$$\Phi_{2,4} = t\kappa e\sin(\omega_0)NC \quad \Phi_{2,5} = -t\kappa\sin(2i)N$$
$$\Phi_{3,1} = -\frac{te(3n + 7\kappa LS)\sin(\omega_0 + \dot{\omega t})}{2\eta}$$
$$\Phi_{3,3} = tA\sin(\dot{\omega t}) + (tB + \eta^2)\cos(\dot{\omega t})$$
$$\Phi_{3,4} = tQ\cos(\dot{\omega t}) + (tB - \eta^2)\sin(\dot{\omega t})$$
$$\Phi_{3,5} = tU\cos(\dot{\omega t}) + tV\sin(\dot{\omega t})$$
$$\Phi_{4,1} = \frac{te(3n - 7\kappa LC)\cos(\omega_0 + \dot{\omega t})}{2\eta}$$
$$\Phi_{4,3} = -tA\cos(\dot{\omega t}) + (tB + \eta^2)\sin(\dot{\omega t})$$
$$\Phi_{4,4} = tQ\sin(\dot{\omega t}) - (tB - \eta^2)\cos(\dot{\omega t})$$
$$\Phi_{4,5} = -tV\cos(\dot{\omega t}) + tU\sin(\dot{\omega t})$$
$$\Phi_{6,1} = \frac{7}{2}t\eta^2\kappa\sin(2i) \quad \Phi_{6,3} = -4te\eta^2\kappa\sin(2i)\cos(\omega_0)$$
$$\Phi_{6,4} = -4te\eta^2\kappa\sin(2i)\sin(\omega_0) \quad \Phi_{6,5} = 2t\eta^2\kappa\sin^2(i)$$
$$M = \eta^3 - \eta - 2 \quad C = 3\cos^2(i) - 1 \quad N = 4\eta^2 + 3$$
$$S = 3\sin^2(i) - 2 \quad L = \eta + 2$$
$$A = 3Ce^2\kappa\cos^2(\omega_0) \quad B = \frac{3}{2}Ce^2\kappa\sin(2\omega_0)$$
$$Q = 3Ce^2\kappa\sin^2(\omega_0)$$
$$U = -3e\kappa\sin(2i)\sin(\omega_0) \quad V = -3e\kappa\sin(2i)\cos(\omega_0)$$

Map between ROE definitions

The map from the EROEs to the ROEs provided in Equation 3 is used frequently in the derivation of STMs. This map is given as

$$\mathbf{M}_{\delta\boldsymbol{\alpha}}^{\delta\boldsymbol{\alpha}^c} = \begin{bmatrix} M_{1,1} & 0 & 0 & 0 & 0 & 0 \\ 0 & M_{2,2} & M_{2,3} & M_{2,4} & 0 & M_{2,6} \\ 0 & M_{3,2} & M_{3,3} & M_{3,4} & 0 & M_{3,6} \\ 0 & M_{4,2} & M_{4,3} & M_{4,4} & 0 & M_{4,6} \\ 0 & 0 & 0 & 0 & M_{5,5} & 0 \\ 0 & 0 & 0 & 0 & 0 & M_{6,6} \end{bmatrix}, \tag{68}$$

with the following substitutions

$$M_{1,1} = \eta^2 \quad M_{2,2} = \frac{1}{\eta} \quad M_{2,3} = -(\eta^2 - \frac{1}{\eta})\frac{\sin(\omega)}{e}$$
$$M_{2,4} = (\eta^2 - \frac{1}{\eta})\frac{\cos(\omega)}{e} \quad M_{2,6} = (\eta^2 - \frac{1}{\eta})\cot(i)$$
$$M_{3,2} = \frac{e_y}{\eta} \quad M_{3,3} = \cos^2(\omega) + \frac{\sin^2(\omega)}{\eta}$$
$$M_{3,4} = (1 - \frac{1}{\eta})\cos(\omega)\sin(\omega) \quad M_{3,6} = -\frac{e_y\cot(i)}{\eta}$$
$$M_{4,2} = -\frac{e_x}{\eta} \quad M_{4,3} = (1 - \frac{1}{\eta})\cos(\omega)\sin(\omega)$$
$$M_{4,4} = \sin^2(\omega) + \frac{\cos^2(\omega)}{\eta} \quad M_{4,6} = \frac{e_x\cot(i)}{\eta}$$

$M_{5,5} = \eta^2 \quad M_{6,6} = \eta^2$

REFERENCES

[1] J. Kruger, A. W. Koenig, and S. D'Amico, "Starling Formation-Flying Optical Experiment (StarFOX): System Design and Preflight Verification," *Journal of Spacecraft and Rockets*, pp. 1–23, Jun. 2023, publisher: American Institute of Aeronautics and Astronautics. [Online]. Available: https://arc.aiaa.org/doi/10.2514/1.A35598

[2] R. Agarwal, B. Oh, D. Fitzpatrick, A. Buynovskiy, S. Lowe, C. Lisy, A. Kriezis, B. Lan, Z. Lee, A. Thomas, B. Wallace, E. Costantino, G. Miner, J. Thayer, S. D'Amico, K. Lemmer, W. Lohmeyer, and S. Palo, "Coordinating Development of the SWARM-EX CubeSat Swarm Across Multiple Institutions," *Small Satellite Conference*, Aug. 2021. [Online]. Available: https://digitalcommons.usu.edu/smallsat/2021/all2021/230

[3] A. W. Koenig, S. D'Amico, and E. G. Lightsey, "Formation Flying Orbit and Control Concept for Virtual Super Optics Reconfigurable Swarm Mission," *Journal of Guidance, Control, and Dynamics*, vol. 46, no. 9, pp. 1657–1670, Sep. 2023. [Online]. Available: https://arc.aiaa.org/doi/10.2514/1.G007334

[4] R. Lillis, S. Curry, C. Russell, J. Luhmann, A. Barjatya, D. Larson, R. Modolo, R. Livi, P. Whittlesey, Y. Harada, C. Fowler, S. Xu, D. Brain, P. Withers, and E. Thiemann, "ESCAPADE: coordinated multipoint measurements of Mars' near-space plasma environment," p. 6354, May 2020, conference Name: EGU General Assembly Conference Abstracts ADS Bibcode: 2020EGUGA..22.6354L. [Online]. Available: https://ui.adsabs.harvard.edu/abs/2020EGUGA..22.6354L

[5] J. L. Burch, T. E. Moore, R. B. Torbert, and B. L. Giles, "Magnetospheric Multiscale Overview and Science Objectives," *Space Science Reviews*, vol. 199, no. 1, pp. 5–21, Mar. 2016. [Online]. Available: https://doi.org/10.1007/s11214-015-0164-9

[6] L. Plice, A. Dono Perez, and S. West, "HelioSwarm: Swarm Mission Design in High Altitude Orbit for Heliophysics," Portland, ME, Aug. 2019, nTRS Author Affiliations: Millennium Engineering and Integration Co. NTRS Report/Patent Number: AAS 19-831 NTRS Document ID: 20190029108 NTRS Research Center: Ames Research Center (ARC). [Online]. Available: https://ntrs.nasa.gov/citations/20190029108

[7] S. D'Amico, A. Koenig, B. Macintosh, and S. Mall, "System Design of the Miniaturized Distributed Occulter/Telescope (mDOT) Science Mission."

[8] J. S. Llorente, A. Agenjo, C. Carrascosa, C. de Negueruela, A. Mestreau-Garreau, A. Cropp, and A. Santovincenzo, "PROBA-3: Precise formation flying demonstration mission," *Acta Astronautica*, vol. 82, no. 1, pp. 38–46, Jan. 2013. [Online]. Available: https://www.sciencedirect.com/science/article/pii/S0094576512002202

[9] C. Lippe and S. D'Amico, "Safe, Delta-v-Efficient Spacecraft Swarm Reconfiguration Using Lyapunov Stability and Artificial Potentials," *Journal of Guidance, Control, and Dynamics*, vol. 45, no. 2, pp. 213–231, 2022, publisher: American Institute of Aeronautics and Astronautics _eprint: https://doi.org/10.2514/1.G006253. [Online]. Available: https://doi.org/10.2514/1.G006253

[10] K. Yamanaka and F. Ankersen, "New State Transition Matrix for Relative Motion on an Arbitrary Elliptical Orbit," *Journal of Guidance, Control, and Dynamics*, vol. 25, no. 1, pp. 60–66, Jan. 2002. [Online]. Available: https://arc.aiaa.org/doi/10.2514/2.4875

[11] O. Montenbruck, M. Kirschner, S. D'Amico, and S. Bettadpur, "E/I-vector separation for safe switching of the GRACE formation," *Aerospace Science and Technology*, vol. 10, no. 7, pp. 628–635, Oct. 2006. [Online]. Available: https://www.sciencedirect.com/science/article/pii/S1270963806000472

[12] M. Willis, "Analytical theory of satellite relative motion with applications to autonomous navigation and control," Ph.D. dissertation, Stanford University, Mar. 2023. [Online]. Available: https://purl.stanford.edu/kq677qp2544

[13] J. Sullivan and S. D'Amico, "Nonlinear Kalman Filtering for Improved Angles-Only Navigation Using Relative Orbital Elements," *Journal of Guidance, Control, and Dynamics*, vol. 40, no. 9, pp. 2183–2200, 2017, publisher: American Institute of Aeronautics and Astronautics _eprint: https://doi.org/10.2514/1.G002719. [Online]. Available: https://doi.org/10.2514/1.G002719

[14] W. H. Clohessy and R. S. Wiltshire, "Terminal Guidance System for Satellite Rendezvous," *Journal of the Aerospace Sciences*, vol. 27, no. 9, pp. 653–658, 1960, publisher: American Institute of Aeronautics and Astronautics _eprint: https://doi.org/10.2514/8.8704. [Online]. Available: https://doi.org/10.2514/8.8704

[15] S. Casotto, "Position and velocity perturbations in the orbital frame in terms of classical element perturbations," *Celestial Mechanics and Dynamical Astronomy*, vol. 55, no. 3, pp. 209–221, Mar. 1993. [Online]. Available: https://doi.org/10.1007/BF00692510

[16] H. Schaub, "Relative Orbit Geometry Through Classical Orbit Element Differences," *Journal of Guidance, Control, and Dynamics*, vol. 27, no. 5, pp. 839–848, 2004, publisher: American Institute of Aeronautics and Astronautics _eprint: https://doi.org/10.2514/1.12595. [Online]. Available: https://doi.org/10.2514/1.12595

[17] S. D'Amico, "Autonomous Formation Flying in Low Earth Orbit," Ph.D. dissertation, Jan. 2010.

[18] A. W. Koenig and S. D'Amico, "Robust and Safe N-Spacecraft Swarming in Perturbed Near-Circular Orbits," *Journal of Guidance, Control, and Dynamics*, vol. 41, no. 8, pp. 1643–1662, 2018, publisher: American Institute of Aeronautics and Astronautics _eprint: https://doi.org/10.2514/1.G003249. [Online]. Available: https://doi.org/10.2514/1.G003249

[19] M. Chernick and S. D'Amico, "New Closed-Form Solutions for Optimal Impulsive Control of Spacecraft Relative Motion," *Journal of Guidance, Control, and Dynamics*, vol. 41, no. 2, pp. 301–319, Feb. 2018. [Online]. Available: https://arc.aiaa.org/doi/10.2514/1.G002848

[20] T. Guffanti, "Optimal passively-safe control of multi-agent motion with application to distributed space systems," Ph.D. dissertation, Stanford University, Jun.

2022. [Online]. Available: https://purl.stanford.edu/gh147jp5825

[21] T. Guffanti and S. D'Amico, "Linear Models for Spacecraft Relative Motion Perturbed by Solar Radiation Pressure," *Journal of Guidance, Control, and Dynamics*, vol. 42, no. 9, pp. 1962–1981, Sep. 2019. [Online]. Available: https://arc.aiaa.org/doi/10.2514/1.G002822

[22] D. Brouwer and G. M. Clemence, "CHAPTER XVI - SECULAR PERTURBATIONS," in *Methods of Celestial Mechanics*, D. Brouwer and G. M. Clemence, Eds. Academic Press, Jan. 1961, pp. 507–529. [Online]. Available: https://www.sciencedirect.com/science/article/pii/B9781483200750500198

[23] J. P. Vinti, *Orbital and Celestial Mechanics*. AIAA, 1998.

[24] J. Neelon, P. Cefola, and R. Proulx, "Current development of the Draper Semianalytical Satellite Theory standalone orbit propagator package," *J. Astronaut. Sci.*, vol. 97, pp. 97–731, Jan. 1997.

[25] A. W. Koenig, "Formation Design of Distributed Telescopes in Earth Orbit with Application to High-contrast Imaging," Ph.D., Stanford University, United States – California, 2019, iSBN: 9798698504245. [Online]. Available: https://www.proquest.com/docview/2466327790/abstract/1FBBD1F2BFD4711PQ/1

[26] D. Brouwer, "Solution of the Problem of Artificial Satellite Theory without Drag," *The Astronomical Journal*, vol. 64, pp. 378–397, 1959. [Online]. Available: https://adsabs.harvard.edu/full/1959AJ.....64..378B7

[27] A. W. Koenig, T. Guffanti, and S. D'Amico, "New State Transition Matrices for Spacecraft Relative Motion in Perturbed Orbits," *Journal of Guidance, Control, and Dynamics*, vol. 40, no. 7, pp. 1749–1768, 2017, publisher: American Institute of Aeronautics and Astronautics _eprint: https://doi.org/10.2514/1.G002409. [Online]. Available: https://doi.org/10.2514/1.G002409

[28] G. E. Cook, "Luni-Solar Perturbations of the Orbit of an Earth Satellite," *Geophysical Journal International*, vol. 6, no. 3, pp. 271–291, Apr. 1962. [Online]. Available: https://doi.org/10.1111/j.1365-246X.1962.tb00351.x

[29] D. A. Vallado, *Fundamentals of Astrodynamics and Applications*. Microcosm Press, 2001, google-Books-ID: OCkGmwEACAAJ.

[30] S. Lowe and S. D'Amico, "REDUCED-ORDER MODEL FOR SPACECRAFT SWARM ORBIT DESIGN."

[31] M. Chernick, "Optimal impulsive control of spacecraft relative motion," Ph.D. dissertation, Stanford University, May 2021. [Online]. Available: https://purl.stanford.edu/vw016ts7713

[32] A. Austin, J. Bapst, B. Bills, A. Berne, C. Bierson, A. Bramson, S. D'Amico, C. Denton, A. Ermakov, A. Evans, D. Hemingway, S. Hernandez, K. Hogstrom, K. Izquierdo, P. James, B. Johnson, M. Kahre, J. Keane, H. Lau, T. Navarro, M. Neveu, F. Nimmo, L. Ojha, H. Paik, J., R. Park, P. Rosen, M. Simons, D. Smith, S. Smrekar, K. Soderlund, M. Sori, G. Steinbrugge, S. Tikoo, N. Wagner, R. Weber, S. Vance, and H. Zebker, "Next Generation Planetary Geodesy," Keck Institute for Space Studies, Tech. Rep., Jun. 2023. [Online]. Available: https://www.kiss.caltech.edu/final_reports/Geodesy_Final_Report.pdf

[33] M. T. Zuber, D. E. Smith, M. M. Watkins, S. W. Asmar, A. S. Konopliv, F. G. Lemoine, H. J. Melosh, G. A. Neumann, R. J. Phillips, S. C. Solomon, M. A. Wieczorek, J. G. Williams, S. J. Goossens, G. Kruizinga, E. Mazarico, R. S. Park, and D.-N. Yuan, "Gravity Field of the Moon from the Gravity Recovery and Interior Laboratory (GRAIL) Mission," *Science*, vol. 339, no. 6120, pp. 668–671, Feb. 2013, publisher: American Association for the Advancement of Science. [Online]. Available: https://www.science.org/doi/full/10.1126/science.1231507

[34] D. Lyons, "Mars Reconnaissance Orbiter: Aerobraking Reference Trajectory," in *AIAA/AAS Astrodynamics Specialist Conference and Exhibit*. American Institute of Aeronautics and Astronautics, _eprint: https://arc.aiaa.org/doi/pdf/10.2514/6.2002-4821. [Online]. Available: https://arc.aiaa.org/doi/abs/10.2514/6.2002-4821

BIOGRAPHY

Nicholas Delurgio *received his B.S. in Aerospace Engineering from the University of Texas at Austin, and is currently pursuing an M.S. in Mechanical Engineering at Stanford University. Nick recently completed an internship at Blue Origin, where he developed attitude guidance and control algorithms for a space mobility vehicle. Previously, he had two internships at Rocket Lab where he designed controllers for spin-stabilized spacecraft and created a monte carlo simulation engine for a lunar lander. Nick's research is focused on developing analytical models and control schemes for close-proximity distributed space systems.*

Simone D'Amico *(Member, IEEE) received the B.S. and M.S. degrees in aerospace engineering from Politecnico di Milano, Milan, Italy, in 2003, and the Ph.D. degree in Aerospace Engineering from the Delft University of Technology, Delft, The Netherlands, in 2010. He is currently an Associate Professor of Aeronautics and Astronautics (AA), W.M. Keck Faculty Scholar in the School of Engineering, and Professor of Geophysics (by Courtesy). He is the Founding Director of the Space Rendezvous Laboratory and Director of the AA Undergraduate Program. Before Stanford, Dr. D'Amico was research scientist and team leader at the German Aerospace Center (DLR) for 11 years. His research aims at enabling future miniature distributed space systems for unprecedented remote sensing, science, exploration and spaceflight sustainability. His efforts lie at the intersection of advanced astrodynamics, spacecraft navigation/control, and space system engineering.*